

This is an Open Access document downloaded from ORCA, Cardiff University's institutional repository: <https://orca.cardiff.ac.uk/id/eprint/125397/>

This is the author's version of a work that was submitted to / accepted for publication.

Citation for final published version:

Gascón, Sergio, Murenu, Elisa, Masserdotti, Giacomo, Ortega, Felipe, Russo, Gianluca L., Petrik, David , Deshpande, Aditi, Heinrich, Christophe, Karow, Marisa, Robertson, Stephen P., Schroeder, Timm, Beckers, Johannes, Irmeler, Martin, Berndt, Carsten, Friedmann Angeli, José P., Conrad, Marcus, Berninger, Benedikt and Götz, Magdalena 2016. Identification and successful negotiation of a metabolic checkpoint in direct neuronal reprogramming. *Cell Stem Cell* 18 (3) , pp. 396-409. 10.1016/j.stem.2015.12.003

Publishers page: <http://dx.doi.org/10.1016/j.stem.2015.12.003>

Please note:

Changes made as a result of publishing processes such as copy-editing, formatting and page numbers may not be reflected in this version. For the definitive version of this publication, please refer to the published source. You are advised to consult the publisher's version if you wish to cite this paper.

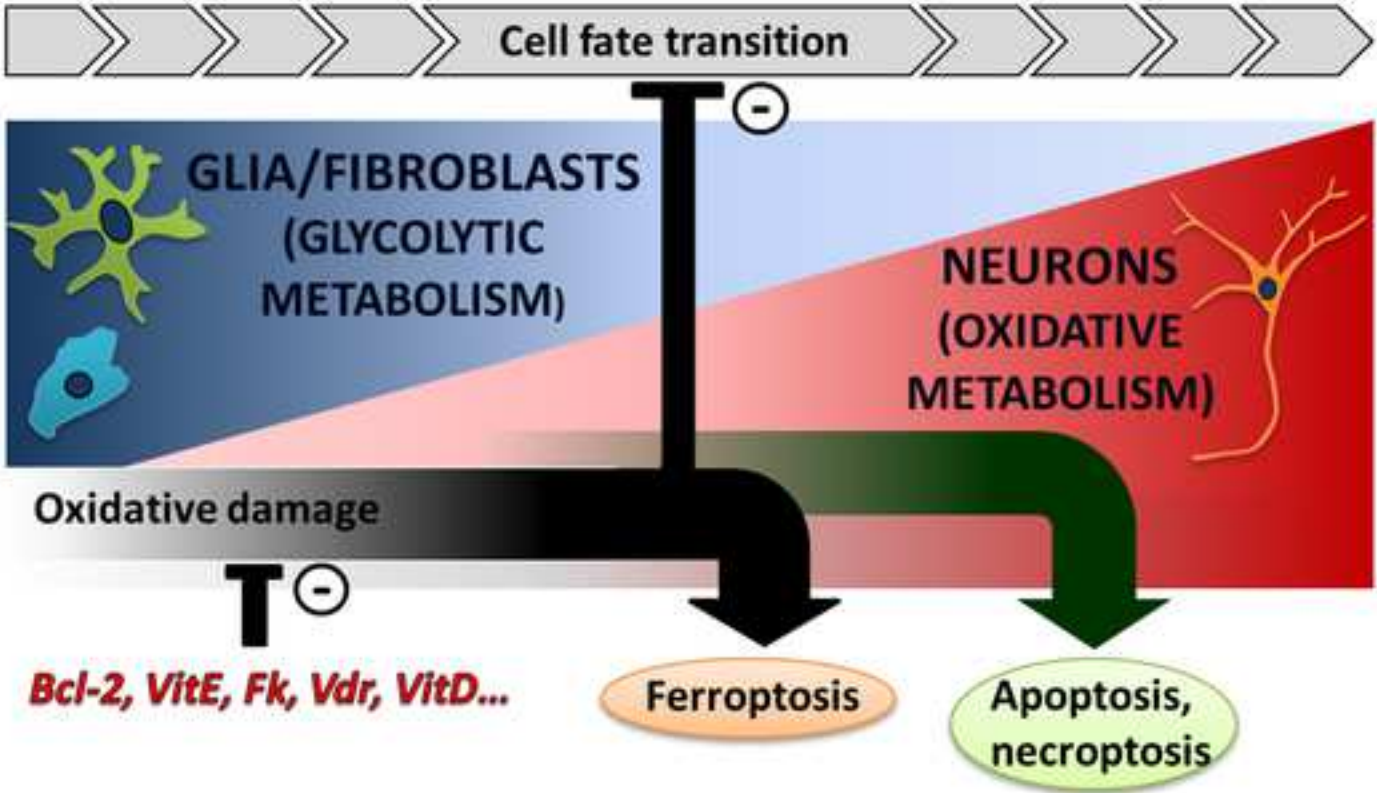
This version is being made available in accordance with publisher policies. See <http://orca.cf.ac.uk/policies.html> for usage policies. Copyright and moral rights for publications made available in ORCA are retained by the copyright holders.



Cell Stem Cell

Identification and successful negotiation of a metabolic checkpoint in direct neuronal reprogramming --Manuscript Draft--

Manuscript Number:	CELL-STEM-CELL-D-15-00452R2
Full Title:	Identification and successful negotiation of a metabolic checkpoint in direct neuronal reprogramming
Article Type:	Research Article
Keywords:	Neuronal reprogramming; brain injury; oxidative stress; lipid peroxidation; Bcl-2; vitamin D; vitamin E
Corresponding Author:	Sergio Gascon Ludwig-Maximilians University München, GERMANY
First Author:	Sergio Gascon
Order of Authors:	Sergio Gascon Elisa Murenu Giacomo Masserdotti Felipe Ortega Gianluca Luigi Russo David Petrik Aditi Deshpande Christophe Heinrich Marisa Karow Stephen Robertson Timm Schroeder Johannes Beckers Martin Irmeler Carsten Berndt José Friedmann Angeli Marcus Conrad Benedikt Berninger Magdalena Götz
Abstract:	<p>Despite the widespread interest in direct neuronal reprogramming, the mechanisms underpinning fate conversion remain largely unknown. Our study revealed a critical time point after which cells either successfully convert into neurons or succumb to cell death. Co-transduction with Bcl-2 greatly improved negotiation of this critical point by faster neuronal differentiation. Surprisingly, mutants with reduced or no affinity for Bax demonstrated that Bcl-2 exerts this effect by an apoptosis-independent mechanism. Consistent with a caspase-independent role, ferroptosis inhibitors potently increased neuronal reprogramming by inhibiting lipid peroxidation occurring during fate conversion. Genome-wide expression analysis confirmed that treatments promoting neuronal reprogramming elicit an anti-oxidative stress response. Importantly, co-expression of Bcl-2 and anti-oxidative treatments lead to an unprecedented improvement in glial-to-neuron conversion after traumatic brain injury in vivo, underscoring the relevance of these pathways in cellular reprogramming irrespective of cell type, in vitro and in vivo.</p>



Identification and successful negotiation of a metabolic checkpoint in direct neuronal reprogramming

Sergio Gascon^{1,2,†,*}, Elisa Murenu^{1,2,†}, Giacomo Masserdotti^{1,2}, Felipe Ortega^{1,3,4}, Gianluca L. Russo^{1,2}, David Petrik^{1,2}, Aditi Deshpande^{1,+}, Christophe Heinrich^{1,°}, Marisa Karow¹, Stephen P. Robertson⁵, Timm Schroeder^{6,#}, Johannes Beckers^{7, 8, 9}, Martin Irmeler⁸, Carsten Berndt¹⁰, José P. Friedmann Angeli¹¹, Marcus Conrad¹¹, Benedikt Berninger^{1,3,12} and Magdalena Götz^{1,2,13,*}

¹ Physiological Genomics, Institute of Physiology, Munich University, Pettenkoferstr.12, 80336 Munich, Germany.

² Institute for Stem Cell Research, Helmholtz Center Munich, Ingolstädterlandstr.1, 85764 Neuherberg/Munich, Germany.

³ Institute of Physiological Chemistry, University Medical Center of the Johannes Gutenberg University, 55128 Mainz, Germany

⁴ Biochemistry and Molecular Biology Department, Faculty of Veterinary medicine, Complutense University, Ave. Puerta de Hierro s/n, 28040 Madrid, Spain

⁵ Department of Women's and Children's Health, Dunedin School of Medicine, University of Otago, Dunedin, New Zealand.

⁶ Research unit Stem Cell Dynamics, Helmholtz Center Munich, Neuherberg, Ingolstädterlandstr.1, 85764 Neuherberg/Munich, Germany

⁷ German Center for Diabetes Research (DZD), 85764 Neuherberg, Germany

⁸ Institute of Experimental Genetics, Helmholtz Center Munich, Ingolstädterlandstr.1, 85764 Neuherberg/Munich, Germany.

⁹ Center of Life and Food Sciences Weihenstephan, Technical University Munich, 85354 Freising, Germany

¹⁰ Department of Neurology, Medical Faculty, Heinrich-Heine University Düsseldorf, Merowingerplatz 1a, 40225 Düsseldorf, Germany

¹¹ Institute of Developmental Genetics, Helmholtz Zentrum München, Ingolstädter Landstr. 1, 85764 Neuherberg, Germany

¹² Focus Program Translational Neuroscience, Johannes Gutenberg University, 55128 Mainz, Germany

¹³ Excellence Cluster of Systems Neurology (SYNERGY), Schillerstr.44, 80336 Munich, Germany.

[†] : both authors contributed equally

present addresses:

⁺ Department of Psychiatry and Institute for Human Genetics, University of California San Francisco, San Francisco, California, United States of America.

[°]Grenoble Institute of Neurosciences Domaine de la Merci. 38042 Grenoble cedex 09, France.

[#]Department of Biosystems Science and Engineering, ETH Zurich, Mattenstr. 26, 4058 Basel, Switzerland.

* corresponding authors:

Sergio.gascon@med.uni-muenchen.de; Magdalena.goetz@helmholtz-muenchen.de

SUMMARY

Despite the widespread interest in direct neuronal reprogramming, the mechanisms underpinning fate conversion remain largely unknown. Our study revealed a critical time point after which cells either successfully convert into neurons or succumb to cell death. Co-transduction with Bcl-2 greatly improved negotiation of this critical point by faster neuronal differentiation. Surprisingly, mutants with

reduced or no affinity for Bax demonstrated that Bcl-2 exerts this effect by an apoptosis-independent mechanism. Consistent with a caspase-independent role, ferroptosis inhibitors potently increased neuronal reprogramming by inhibiting lipid peroxidation occurring during fate conversion. Genome-wide expression analysis confirmed that treatments promoting neuronal reprogramming elicit an anti-oxidative stress response. Importantly, co-expression of Bcl-2 and anti-oxidative treatments lead to an unprecedented improvement in glial-to-neuron conversion after traumatic brain injury *in vivo*, underscoring the relevance of these pathways in cellular reprogramming irrespective of cell type, *in vitro* and *in vivo*.

INTRODUCTION

Direct reprogramming of somatic cells has proven to be an extraordinary method to generate cell populations such as neurons that are otherwise difficult to obtain, for research purposes (Amamoto and Arlotta, 2014). In addition, replenishing neuronal populations in the injured brain using reprogramming-based therapies is an exciting future prospect (Buffo et al., 2005; Heinrich et al., 2014). However, the cellular and molecular basis underlying direct reprogramming remains poorly understood. Most studies are restricted to the function of neurogenic reprogramming factors (Masserdotti et al., 2015; Ninkovic et al., 2013; Wapinski et al., 2013), while little is known about other aspects, such as metabolic changes or proliferation. As the function of neurogenic factors is context-dependent, this also prompts the question to which extent there may be mechanisms common to all cells types converting into neurons. For example, Neurogenin2 (Neurog2) efficiently induces neuronal conversion of mouse postnatal astrocytes in culture (Berninger et al., 2007; Blum et al., 2011; Heinrich et al., 2010) but is rather ineffective in mouse embryonic fibroblasts (MEFs) (Chanda et al., 2014) or adult reactive glial cells *in vivo* (Grande et al., 2013). While the starting cell type may dictate conversion efficiency by providing transcriptional accessibility of target genes (Wapinski et al., 2013), other cellular processes shown to influence reprogramming into induced pluripotent stem cells (iPSCs) such as cell death (Kawamura et al., 2009),

proliferation rate (Halley-Stott et al., 2014; Ruiz et al., 2011) or metabolic state (Zhang et al., 2012), may also be important in direct neuronal reprogramming. Among them, the metabolic state is particularly relevant for the conversion into neurons, which rely on oxidative metabolism, while astroglia, fibroblasts and proliferative cells rather utilize anaerobic glycolysis and β -oxidation (McKay et al., 1983; Tsacopoulos and Magistretti, 1996). Moreover, metabolic factors such as reactive oxygen species (ROS) have been implicated in cell fate regulation (Maryanovich and Gross, 2013). Here, we used continuous single cell live imaging to monitor direct reprogramming of fibroblasts and glia into neurons. We identify stage specific barriers and metabolic regulators increasing conversion efficiency both in vitro and in vivo.

RESULTS

A Critical Checkpoint Eliciting Cell Death in Neuronal Conversion

To target also postmitotic cells, we transfected astroglial cells isolated from mouse cerebral cortex at postnatal day (P) 5-7 with a dual red fluorescent protein (RFP) and *Asc11*-encoding vector (Heinrich et al., 2010; Masserdotti et al., 2015) and tracked RFP+ cells starting at 26-29 hours after transfection (Figure 1A). In this model, neuronal conversion is achieved within 7 days, and can be monitored by continuous single cell imaging. Images were taken every 5 minutes in phase contrast and 5 hours in the fluorescence channel (RFP+; Movie S1; Figure 1B shows stills from such movies). To follow the fate conversion we used 3 methods: neuronal morphology (Movie S1, Figure 1B-H and Figure S1A), GFP driven by the Doublecortin promoter (*DCX-GFP*; Movie S2, Figure S2A-C), and immunostaining for neuron-specific antigens (Figure S2D, E). The first signs of neuronal conversion were visible by weak *DCX-GFP* signals at around 24 hours of live imaging (Figure S2A1, B1, H-blue line; i.e. about 2 days after transfection, see Figure 1A) and most cells that became *DCX-GFP*+ did so within the first 2 days of imaging (Figure S2A1, B1, C-blue line), i.e. about 3 days after transfection (Figure 1A). Thus, the regulation of key neuronal genes occurs rapidly and is implemented within few days (see also (Masserdotti et al., 2015)). Within 50 hours of imaging, i.e. about 3 days after transfection, the first

Ascl1/RFP+ cells changed from flat astrocyte to neuronal morphology (Figure 1B1, C1). Noteworthy, more than 90% of cells classified with a neuronal morphology were accordingly immuno-reactive for β -III-tubulin and MAP2. The more mature neuronal marker NeuN was present in only in 60% of cells with neuronal morphology (Fig. S1B, C). Among the cells with non-neuronal morphology we found cells in fate transition immunoreactive for both neuronal (β -III-tubulin) and astroglia (GFAP) markers (Figure S1E, upper panels). Cells with a neuronal morphology were never found to be double-positive for GFAP and neuronal markers (Figure S1E, lower panels), confirming the stringency of these criteria. By about 150 hours of imaging (7 days post-transfection, DPT) most RFP+ cells had developed a neuronal morphology (Figure 1B1, C1 and D, left bars) or DCX-reporter activity (see example in Figure S2A1, B1, C-blue line). However, at that time the number of RFP+ cells had decreased dramatically, with only about 18% of all RFP+ cells observed at the beginning of the time lapse (see Movie S1) surviving to the end (Figure 1B1, C1, D, left bars). The peak of cell death occurred between 50-100 hours imaging (Figure 1B1, C1, D, left bars), when fate conversion manifests by morphological changes (Figure 1B1, C1). Most (94%) transfected cells that did not acquire a neuronal morphology underwent cell death at some point during the observation period (Figure 1D, G, left bars), while only 48% of the cells with neuronal morphology died (Figure 1H, left bar). Accordingly, most cells surviving until the end of imaging were reprogrammed into neurons (Figure 1B1, C1, D, left bars; Figure S2A1, B1, C-blue line). Thus, cell death is a main limiting factor of neuronal reprogramming and peaks at the time of fate conversion. Conversely, proliferation is limited in this paradigm (Figure 1F, left bar) with most astrocytes directly converting into neurons (Figure 1C1).

Bcl-2 improves fate conversion and survival

To improve survival during reprogramming, we first examined the effect of the anti-apoptotic protein Bcl-2. Indeed, co-expression of *Bcl-2* with *Ascl1/RFP* in astrocytes not only increased the total number of surviving cells, but also the number of induced neurons (iN), based on morphological analysis (Figure 1B-D), DCX-reporter activity (Figure S2A-C) and immunostaining for β -III-tubulin and MAP2

at 5 days DPT (Figure S2D, E). Furthermore, continuous single cell imaging revealed a faster conversion of *Ascl1/Bcl-2* co-transfected astrocytes, with a significant increase in the proportion of cells with neuronal morphology in the initial phases (8-fold at 50h of tracking time; Movie S1, Figure 1C-E) and faster acquisition of DCX-reporter (Movie S2, Figure S2A-C) but no effect on cell proliferation (Figure 1F). *Bcl-2* expression increased the proportion of surviving cells in the whole transfected population (Figure 1B-D; Figure S2A-C), while each class of cells, i.e. those with neuronal and non-neuronal morphology, still died as much as cells not co-expressing *Bcl-2* (Figure 1G, H). Thus, the main effect of *Bcl-2* is to facilitate fate transition from astrocytes to neurons, which then have a lower death rate (Fig. 1I).

Continuous live imaging results were further corroborated by immunostaining and electrophysiology. Indeed, neuronal morphology faster acquired by *Bcl-2* co-expression correlated with lower resting membrane potential (RMP=-60 to -40 mV; Figure S2F, G) typical for immature neurons (Pedroni et al., 2014), while astrocytes have a RMP of -90 to -80 mV (Anderova et al., 2004) (Figure S2F, G). Notably, at 5DPT, when most reprogrammed cells have already acquired DCX-GFP, β -III-tubulin, MAP2 and NeuN expression (Figure S1C, D), their electrophysiological properties are still immature and only 10% of *Ascl1/Bcl-2* co-transfected cells exhibited some very immature action potential-like features (Figure S2F3). However, iNs recorded at 15 DPT showed action potentials consistent with fully developed neurons (Figure S2H). Taken together, these results demonstrate that *Bcl-2* improves reprogramming by faster fate conversion.

Bcl-2 Promotes the Efficiency of Neuronal Conversion Via a Non-Canonical Pathway

As the *Bcl-2* effect seems not only related to its anti-apoptotic role, we examined the contribution of its canonical function via the interaction with the pro-apoptotic Bax/Bak. *Bcl-2* inhibits apoptosis by sequestering Bax/Bak when phosphorylated at serine 69/70 (Deng et al., 2006) (Figure 2A). The replacement of both Ser69/70 by glutamic acid (EE-*Bcl-2*) mimics the constitutively phosphorylated form of *Bcl-2*, that sequesters Bax (Figure 2A), while substitution of Ser70 by alanine (A(70)-*Bcl-2*;

Figure 2A) mimics the un-phosphorylated form of Bcl-2, reducing the binding to Bax (Deng et al., 2006). Likewise, A(145)-Bcl-2 is unable to bind Bax due to a Glycine145/alanine substitution (Figure 2A; Yin et al., 1994).

Co-expression of EE-*Bcl-2* increased survival of cells transfected with *Ascl1* (Figure 2B), but did not alter the proportion of iNs (blue bars in Figure 2C). As expected, A(145)-Bcl-2 had no significant effect in promoting cell survival during reprogramming (Figure 2B), but surprisingly still increased the proportion of *Ascl1*-transfected cells that turned into neurons (blue bars in Figure 2C). Co-transduction with A(70)-*Bcl-2* still retained some effect on cell survival (comparable to WT-*Bcl-2*, Figure 2B) and was most efficient in neuronal conversion, due to the added effect of rescuing non-converted cells from death and allowing them to convert more efficiently (Figure 2C, grey and blue bars respectively). Moreover, we also observed increased length and complexity of the neuronal processes in cultures co-transfected with wild type (WT)-*Bcl-2*, A(70)-*Bcl-2* or A(145)-*Bcl-2* but not with EE-*Bcl-2* (Figure 2D), further supporting an additional non-apoptotic role of Bcl-2 in neuronal reprogramming.

Importantly, Bcl-2 also enhanced conversion efficiency obtained from astrocytes transduced with *Neurog2* (Figure 2E), which induced mature glutamatergic neurons (vGlut1+ cells, Figure 2F). Both WT-*Bcl-2* and, to a greater extent, A(70)-*Bcl-2* potentially enhanced reprogramming of mouse embryonic fibroblasts (MEFs) in combination with a single neurogenic fate determinant (*Ascl1*, Figure 2H, I and Figure S3A, C; *Neurog2*, Figure S3B, E, F) giving rise to functional neurons able to fire action potentials (Figure S3D). Notably, Bcl-XL, a member of the Bcl-2 family, had a similar effect on reprogramming as WT-*Bcl-2* (data not shown). However, in the absence of a neurogenic factor neither A(70)-*Bcl-2* nor any other *Bcl-2* construct nor *Bcl-XL* alone were able to induce neuronal conversion (Figure 2G and Figure S3C and data not shown). We thus conclude that Bcl-2-related proteins act as a potent facilitators of direct neuronal reprogramming for different transcription factors in different cell types and does so most potently in the A(70)-Bcl-2 mutant form.

Mode of Cell Death in Neuronal Reprogramming

As EE-Bcl-2, the mutant which exhibits an improved anti-apoptotic function, increases cell survival but does not improve the proportion of iNs, we tested how different modes of cell death affect neuron numbers. The pan-caspase/apoptosis inhibitor Z-VAD-FMK (ZVAD, 20 μ M) was added once at day 2 to *Ascl1*-transfected astrocytes, resulting in a significant increase in surviving cells (Figure 3A) without affecting the proportion of iNs neither amongst the initially transfected cells (Figure 3B, grey bars) nor at the end point (Figure 3B, blue bars). Thus, like EE-Bcl-2, blocking caspase activation does not improve neuronal conversion. We then tested the effects of RIP-K dependent necroptosis and the oxidative stress-dependent ferroptosis (Dixon et al., 2012) by using their respective inhibitors Necrostatin-1 (Degterev et al., 2005) and Liproxstatin-1 (Friedmann Angeli et al., 2014). While Necrostatin-1 had similar effects to ZVAD in rescuing some cells from death (Figure 3A), but no effects on iNs (Figure 3B), Liproxstatin-1 had a potent effect on conversion efficiency (Figure 3B). Thus, while apoptosis and necroptosis inhibitors protect cells from death, only the ferroptosis inhibitor liproxstatin-1 promotes both survival and neuronal conversion.

Increased Lipid Peroxidation During Neuronal Reprogramming

Given the positive effects of Liproxstatin-1 treatment on reprogramming efficiency, we next examined lipid peroxidation (Lip-Ox) as a hallmark of ferroptosis (Dixon et al., 2012) by using two different reporters: Click-iT lipid peroxidation kit based on linoleamide alkyne (LAA) reagent (Life technologies) and C11-Bodipy (Drummen et al., 2002). Astrocyte cultures treated with cumene hydroperoxide as a positive control for Lip-Ox had increased signal from the LAA-based reporter in almost all cells (Figure 3C, upper row). Without any additional treatment, 60% of *Ascl1*-transfected cells exhibited the signal for Lip-Ox at 3 DPT, in contrast to 25% of cells transfected with the control plasmid (Figure 3C, D), suggesting that Lip-Ox occurs primarily during neuronal reprogramming. Similar results were obtained with C11-Bodipy, which integrates into phospholipid-containing membranes and shifts from red to green fluorescence upon oxidation (Drummen et al., 2002). We also tested α -Tocopherol (α Toc, one of the forms of Vitamin E, 20 μ M), known to protect against Lip-Ox

(Buettner, 1993), and found that it strongly reduces Lip-Ox LAA-signal in astrocytes undergoing neuronal conversion (Figure 3C, D).

Given the non-canonical effect of Bcl-2 on neuronal reprogramming, we examined its effect on Lip-Ox. Indeed, all forms of Bcl-2 significantly reduced Lip-Ox with EE-Bcl-2 being the weakest and A(70)-Bcl-2 the strongest (Figure 3D). This result was observed with both reporters (Figure 3D, E), demonstrating a novel role of Bcl-2 in protecting from Lip-Ox most potently in the A(70)-Bcl2 mutant form. Consequently, we hypothesized that any condition that reduces Lip-Ox should be beneficial for direct neuronal reprogramming. Indeed, α Toc treatment, almost doubled the proportion of *Ascl1/RFP* reprogrammed neurons obtained from astrocytes at 5DPT (Figure 4A-C) and improved conversion efficiency of cells co-treated with ZVAD or co-expressing *Ascl1/EE-Bcl-2* (Figure 4A, B). Thus, the anti-oxidant Vitamin E improves direct neuronal reprogramming.

Forskolin Promotes the Efficiency of Neuronal Conversion and Reduces Lipid Peroxidation

We next tested if other molecules known to improve reprogramming such as Forskolin (Fk; Liu et al., 2013a) may also alleviate Lip-Ox. First we verified its positive effects on reprogramming in astrocytes aiming to determine if it would act similarly from what we had observed with Bcl-2. Both in continuous live imaging (Figure S4A-D) and after immunostaining at 5DPT (Figure 4D, E) we observed more cells surviving and efficiently converting after addition of 20 μ M forskolin to *Ascl1*-transfected astrocyte cultures. As for Bcl-2, we also observed a faster conversion (Figure S4A-D) without any effect on proliferation (Figure S4E). This effect is both transcription factor and cell type independent, as Fk also improved reprogramming efficiency of MEFs and pericytes (Figure S5) mediated by different transcription factors (i.e, *Ascl1*, *Neurog2*, *Sox2*) but did not induce neuronal conversion in absence of any neurogenic fate determinant (Figure S4F and S5C).

As expected, the proportion of Lip-Ox reporter-positive cells among *Ascl1*-transduced astrocytes was significantly reduced from about 60% to below 20% by Fk treatment (Figure 4F, G). Likewise, CellRox Green reagent (Molecular probes; Figure 4H) showed high levels of nuclear green

fluorescence in *Ascl1* transduced astrocytes at 3DPT, when many cells succumb to cell death, which was reduced after Fk treatment (Figure 4H). As further proof of oxidation-dependent processes occurring during reprogramming, we monitored the oxidation of peroxiredoxin-2, a protein involved in oxidative stress detoxification (Prx2; Godoy et al., 2011), by Western Blot. Prx2 was predominantly detected in its dimeric (oxidized) form in astrocytes and MEFs 3 days after transduction with *Ascl1*, and dimerization was reduced by Fk treatment (Figure 4I). Thus, reducing oxidative stress during reprogramming facilitates neuronal conversion.

Genome-Wide Expression Analysis Reveals Anti-Oxidative Stress Response in Improved Neuronal Reprogramming

To identify candidate genes regulated by non-canonical Bcl-2 function and by Fk treatment that may promote neuronal conversion, we collected mRNA from different batches of MEF cultures. These were transduced with *Ascl1/RFP*- or *RFP*-encoding vectors and treated or untreated with Fk for 24 hours (1DPT) or co-transduced with A(70)-*Bcl-2-GFP* (Figure 5A). Upon Fk treatment 507 probe-sets were significantly regulated ($p < 0.01$, fold change $\geq 1.5x$, see Table S1; for genes regulated after A(70)-*Bcl-2* co-transduction see Table S2). Heat maps show the 60 strongest up-regulated genes upon Fk treatment of *Ascl1* transduced cells (Figure 5B, left panel) and the subset of transcriptional regulators (right panel). The reliability of the transcriptome analysis was confirmed by quantitative real-time PCR analysis (Figure 5C). As expected from the known role of Fk we found increased expression of genes involved in the cAMP signalling-pathway (Table S3) and many targets of Creb, including those regulating neurite outgrowth and cAMP-signalling mediators (Tables S1, S3), as well as genes promoting neuronal differentiation (e.g. *Prox1*, *Eya2*, *Sox11*; Figure 5B). In addition, we found enrichment of several signalling pathways (e.g. IL-10 & IL-1; Wnt, Bmp) and nuclear receptors (Figure 5B and Table S3). Interestingly, some of these genes, including Nrf-2 effectors and JAK/STAT (Table S1, S3) are known to regulate metabolism and the oxidative stress response (Nguyen et al., 2009; Park et al., 2012). GO term analysis further supported anti-oxidative pathways activated by Fk, with Nrf2-

mediated pathway at the top (Table S3). Indeed, we confirmed increased Nrf2 responsive luciferase activity 15h after Fk addition (Figure 5D). Interestingly, Nrf2-mediated pathway was found activated by both Fk treatment and A(70)-Bcl-2 co-expression (Table S4). These data support the notion of excessive oxidation occurring during reprogramming and Fk as well as A(70)-Bcl-2 alleviating this. As Vitamin D receptor (Vdr) was already implicated in the anti-oxidative stress response (Bao et al., 2008; Dong et al., 2012), we validated its up-regulation at mRNA level in MEFs and astrocytes (Figure 5E; see also confirmation of other nuclear receptors) and protein level in astrocytes (Figure 5F). We then tested its effect on Lip-Ox in astrocytes and found that co-expression of *Vdr* reduced the percentage of cells positive for LAA-based reporter to less than 1/3 in *Ascl1*-transfected astrocytes at 3.5 DPT (Figure 5G). Accordingly, co-transfection with *Vdr* improved neuronal reprogramming by *Ascl1* or *Neurog2* to a similar extent as Fk (data not shown) or *Bcl-2* co-transfection (Figure 5H-K). Co-transduction of *Bcl-2* and *Vdr* further increased reprogramming (Figure 5H-K) reaching up to 80% neurons amongst *Ascl1*-transduced astrocytes (Figure 5H, J). Taken together, genome-wide expression analysis confirmed the key role of oxidative stress response in regulating reprogramming, with Vdr as the top transcriptional regulator.

The Role of Bcl-2 and Anti-Oxidants in Neuronal Reprogramming *In Vivo*

We next examined the relevance of the above identified pathways after brain injury *in vivo*. Such lesions induce a highly inflammatory environment (Abdul-Muneer et al., 2014) that may impose oxidative stress and other metabolic constraints to the generation and survival of iNs. Indeed, in the intact striatum and cerebral cortex neuronal reprogramming was more efficient (Guo et al., 2014; Niu et al., 2013; Torper et al., 2013) than after large invasive brain injury (Grande et al., 2013; Heinrich et al., 2014). Among the previously tested factors we chose *Neurog2*, as it instructs glutamatergic neurons in the developing cerebral cortex (Imayoshi and Kageyama, 2014) from astrocytes *in vitro* (Berninger et al., 2007; Heinrich et al., 2010; Masserdotti et al., 2015), but exhibits a limited efficiency in neuronal conversion after brain injury *in vivo* (Grande et al., 2013).

Retroviral vectors encoding *Neurog2*-IRES-*RFP* alone or in combination with *Bcl-2*-IRES-*GFP* were injected close to the stab-wound injury site 3 days later (Figure 6A) as previously described (Buffo et al., 2005; Heinrich et al., 2014) and immunohistochemistry was performed at 10 days post-injection (DPI). *GFP* or *Bcl-2* single (*GFP*⁺) infected cells were NG2⁺ glia or S100 β /GFAP⁺ astrocytes (Figure 6C and S6C). Similarly, most of the cells transduced with *Neurog-2* (*RFP*⁺ only) were glia and only rarely acquired the neuronal marker NeuN (Figure 6B, C, F; 2% in only *Neurog2* infected brains, Figure S6D). Conversely, many co-transduced cells (*GFP*⁺/*RFP*⁺) exhibited elongated neuronal-like morphology and were immuno-reactive for DCX or NeuN (Figure S6E, Figure 6C). Indeed, around 75% of co-transduced cells had turned into NeuN⁺ neurons with a clear neuronal morphology at 10 DPI (Figure 6F). Taken together, addition of *Bcl-2* not only increased the number of NeuN⁺ iNs but also accelerated neuronal maturation, as appearance of NeuN typically takes about 14-21 DPI (Grande et al., 2013). Thus, as *in vitro*, *Bcl-2* potently improves reprogramming speed and efficiency *in vivo*.

We next examined whether activating the Vdr pathway by the ligand calcitriol after *Neurog2/RFP* transduction with/without *Bcl-2/GFP* would elicit a further improvement in reprogramming. Strikingly, a single calcitriol administration at 2 DPI more than doubled the proportion of NeuN⁺ iNs in *Neurog2* transduced cells (Figure 6D, F; 3.5-fold increase in only *Neurog2* infected brains, see Figure S6D). Most importantly, calcitriol treatment resulted in almost 90% conversion of all *Neurog2/Bcl-2* co-transduced cells (*GFP*⁺/*RFP*⁺; Figure 6D, F), dramatically increased levels of NeuN (see Figure S6F, G) and improved morphology and complexity of iNs, resulting in the formation of long neuronal processes (Figure S6G). Moreover, long-term analysis of iNs after calcitriol treatment often revealed very elaborate neurites with bouton- (20 DPI, Figure 6G) and/or spine-like structures (60 DPI, Figure 6H). Taken together, these data demonstrate that calcitriol has a beneficial effect on the reprogramming efficiency but more importantly, on the maturation of iNs.

To confirm that the oxidative state directly affects reprogramming *in vivo*, we administered α -Tocotrienol (α T3; Figure 6A), the vitamin E analogue described above. Similarly to calcitriol, α T3 administration improved the conversion efficiency and the levels of NeuN (Figure 6E, F). Strikingly,

cells co-transduced with *Neurog2/Bcl-2* displayed a very complex neuronal morphology in animals treated with α T3 already at 10 DPI (Figure 6E and 7A) and had a soma size comparable to the endogenous neurons in the same area (Figure 7A, B). Notably, iNs also reached this soma size after calcitriol administration, but at a much later time points (60 DPI, see Figure S6H and 7A). Likewise, upon α T3 treatment iNs exhibited the first spine-like protrusions already at 10 DPI (Figure 7A, left panels), further corroborating the faster iN differentiation and maturation elicited by this anti-oxidant. As *Neurog2/Bcl-2* over-expression and α T3 administration resulted in most developed iNs, we used this paradigm to determine their subtype identity. Regardless of the localisation of the co-transduced cells, about 80% were immunopositive for Ctip2 (Figure 7D, G), a marker for layer 5 subcortical neurons (Arlotta et al., 2005; Molyneaux et al., 2007). Most of the remainder (20%) were positive for the deep layer marker FoxP2, albeit with lower intensity than endogenous neurons (Figure 7C, G; Molyneaux et al., 2007). Consistent with a layer 5 pyramidal neuron identity, iNs were negative for the upper layer markers Satb2 (Figure 7F left panels, G; Britanova et al., 2008) or Cux1 (Figure 7F right panels, G; Nieto et al., 2004) and the interneuron transmitter GABA (Figure 7E). Therefore, we confirmed the identity of reprogrammed cells as deep layer glutamatergic pyramidal neurons, consistent with the role of *Neurog2* in cortical development (Schuurmans et al., 2004).

DISCUSSION

Here we used continuous live imaging to unravel critical hurdles in direct neuronal reprogramming. Neuronal conversion became detectable around 2-4 days after transduction by live neuronal (DCX-*GFP*) reporters, post-imaging immunostaining (β -III-tubulin, MAP2, NeuN) and morphological analysis (small cell soma and thin processes). At around the same time, most transduced astrocytes succumbed to cell death, while fewer of the successfully converted cells died, suggesting that high levels of *Ascl1* may be incompatible with astrocyte survival under these conditions. Importantly, few astrocytes proliferated – neither prior to cell death nor prior to fate conversion. Thus, a major limitation in reprogramming efficiency is cell death around the time of fate conversion.

Different Modes of Cell Death and Oxidative Stress Limit Neuronal Reprogramming

While blocking apoptosis by caspase inhibitors and necroptosis by RIPK1 inhibitors significantly increased cell survival, these cell death pathways did not affect the proportion of iNs. This revealed an additional block for neuronal conversion that could be consistently relieved by ferroptosis inhibitors (Liproxstatin-1 or Vitamin E). Ferroptosis is typically induced by ROS resulting in peroxidation of lipids due to impaired cysteine availability, glutathione depletion and GPX4 inhibition (Dixon et al., 2012; Friedmann Angeli et al., 2014; Yang et al., 2014). Hence, excessive ROS may be generated as a consequence of instructing reprogramming *per se* or specifically into neurons, that use oxidative phosphorylation. In favour of the former possibility are the findings of an oxidative burst with deleterious consequences during the generation of mouse iPSCs (Kida et al., 2015; Qi et al., 2015), initiated when cells are instructed to divide fast during reprogramming (Kida et al., 2015). This is notably different from direct neuronal reprogramming, where few cells divide and yet increased ROS and Lip-Ox occur. We therefore favour the hypothesis that this effect is due to transitioning too hastily to the neuronal oxidative metabolism during reprogramming (see also below).

Consistent with high oxidation levels limiting neuronal reprogramming efficiency, we show here that treatments beneficial for reprogramming, such as Fk or A(70)-Bcl-2, reduce Lip-Ox and mount an anti-oxidative response mediated by Nrf2 amongst others. Various agents attenuating Lip-Ox, such as α Toc, α T3 or Calcitriol, also improve neuronal reprogramming. This is not only of crucial importance to better understand the conversion process into iNs but also for the wide-spread application of generating neurons from different cell types (astrocytes, MEFs, pericytes etc.) with various neurogenic transcription factors (Ascl1, NeuroD4, Neurog2, Sox2 etc) at much increased efficiency.

An Un-expected Role for Bcl-2 In Direct Neuronal Reprogramming

Interestingly, Bcl-2 affected both reprogramming efficiency and speed of neuronal conversion in a manner un-coupled from its function in apoptosis. The Bcl-2 mutant with increased affinity for

Bax/Bak and therefore improved anti-apoptotic function (EE-*Bcl-2*) neither improved neuronal reprogramming nor reduced Lip-Ox. In contrast, A(145) and A(70)-*Bcl-2* mutants, unable to bind Bax/Bak and with reduced anti-apoptotic function (Deng et al., 2006; Yin et al., 1994) improved neuronal reprogramming, with the latter being the most effective in reducing Lip-Ox and, consequently, enhancing reprogramming efficiency. While this is the first time that specific *Bcl-2* mutants have been used to assess selective effects on Lip-Ox, *Bcl-2* has formerly been implicated in the regulation of both metabolic transition and oxidative stress pathways, by reducing oxidation in mitochondria (Krishna et al., 2011) or improving metabolic conversion via interaction with e.g. p53 or Myc (Deng et al., 2006; Jin et al., 2006). As EE-*Bcl-2* interacts strongly with Bax, its lack of effect on reprogramming could be due to its reduced availability for molecular partners acting in the nucleus. Conversely, A(70)-*Bcl-2* may be more efficient in improving neuronal reprogramming as more of this protein may be available in the nucleus for interaction with relevant partners.

Notably we show that Fk and A(70)-*Bcl-2* lead to common transcriptional changes in pathways (e.g. LXR) that have been previously implicated in neurogenesis (Theofilopoulos et al., 2013), suggesting that nuclear interactions of *Bcl-2* may explain the particular efficiency of the A(70)-*Bcl-2* mutant in direct neuronal reprogramming. Although not precluding additional roles of *Bcl-2* at the mitochondria or other mechanisms, our data demonstrate that the effect of *Bcl-2* in reprogramming is independent of its well-known anti-apoptotic function.

Metabolic Conversion as Critical Factor in Direct Neuronal Reprogramming

Importantly, factors alleviating Lip-Ox also accelerate fate transition. We observed this *in vivo* and by continuous single cell tracking analysis *in vitro*, both upon Fk treatment and in cells co-expressing *Bcl-2* (Figure 1 and Figure S3). Fk treatment regulates several genes affecting the cellular redox potential, e.g. *Nor-1* that promotes the endurance phenotype in oxidative muscle fibers (Pearen et al., 2012) and *Vdr* that alleviates oxidative stress in various organs (Dong et al., 2012; George et al., 2012). It has been previously shown that ROS and redox-signaling mechanisms play a key role in cell fate decisions

including neurogenesis (Maryanovich and Gross, 2013; Prozorovski et al., 2015), although the molecular mechanisms mediating these effects are not yet fully understood. In iPSC reprogramming, changes to a more glycolytic metabolism have been shown to govern fate conversion (Liu et al., 2013b), despite the initial oxidative burst mentioned above (Kida et al., 2015). The faster neuronal conversion when excessive oxidation products are successfully controlled is consistent with a) ROS affecting gene expression, e. g. by altering SIRT activity, a key regulator of neurogenesis and b) interfering with metabolic pathways acting up-stream of other aspects of fate conversion. If the metabolic transition is a pre-requisite for the conversion in cell fate, redox homeostasis failure may ultimately reduce efficiency or speed of conversion.

Confirming this hypothesis, we observed that cells cultured in a medium with oligomycin A, allowing anaerobic glycolysis as the only metabolic pathway to generate ATP (see Suppl. Material), preserved astroglial features and interfered with the conversion to a neuronal fate (Figure S7A-C,E-F). As the total cell number did not decrease much (Figure S7A, F), fate conversion seems to be blocked when oxidative phosphorylation is hampered. Notably, cells grown in anaerobic glycolysis-only medium were also protected from Lip-Ox (Figure S7C, D), demonstrating that the metabolic change during neuronal reprogramming causes oxidative stress. Conversely, boosting the metabolic shift with a medium containing 2-deoxy-glucose, which can only be metabolized at mitochondria (see Suppl. Material), caused extraordinarily high levels of Lip-Ox (Figure S7C) in astrocytes and resulted in cell death (Figure S7A, F). Overall, these experiments demonstrate that the metabolic shift is not only necessary to allow survival of the neurons during reprogramming but also constitutes a pre-requisite for cell fate transition.

Potent Improvement of Direct Reprogramming in the Injured Brain *In Vivo*

Importantly, α T3 supplementation or activation of anti-oxidant pathways by calcitriol was remarkably powerful in improving iN maturation from reactive glia after traumatic brain injury *in vivo*. Interestingly, calcitriol treatment has been shown to reduce glutamate-induced neuronal death *in vitro*

and attenuate hypoxic brain damage *in vivo* (Gianforcaro and Hamadeh, 2014), as well as the fibrotic reaction upon injury in other organs (Ding et al., 2013; Sherman et al., 2014). These data thus suggest that calcitriol alleviates several negative effects after injury. While both calcitriol and α T3 also improve efficiency of reprogramming but predominantly affect maturation and neurite growth, *Bcl-2* co-expression was the most efficient in increasing iNs. The combined action of *Bcl-2* and Calcitriol or α T3 allowed us for the first time to achieve an *in vivo* reprogramming efficiency of more than 90% after stab wound injury. The neurons survived for several months and acquired a remarkably advanced state of maturation. These data demonstrate that the number of neurogenic fate determinants was not the limiting factor in neuronal reprogramming after injury *in vivo*, as believed so far. In fact, while applying various combinations of neurogenic transcription factors only marginally improved reprogramming in the same paradigm (Buffo et al., 2005; Grande et al., 2013; Heinrich et al., 2014; Kronenberg et al., 2010), co-expressing *Bcl-2* and alleviating excessive ROS had an astounding effect. Indeed, our protocol allowed iNs to proceed largely to a specific neuronal subtype, namely *Ctip2*+ pyramidal neurons even when they were located at more superficial positions and surrounded by *Cux1*+ upper layer neurons. Interestingly, *Ctip2* is not a direct target of *Neurog2* (Masserdotti et al., 2015; Schuurmans et al., 2004) and acts as the key effector of subcortical deep layer neuron fate (Amamoto and Arlotta, 2014). Moreover, *Neurog2* knock-out mice have selective defects in deep layer, but not upper layer neurons of the developing cerebral cortex (Fode et al., 2000) supporting the concept that *Neurog2* is largely involved in specifying deep layer neuron fate in this region.

Taken together, our data on the mechanisms facilitating the metabolic transition and redox homeostasis in neuronal reprogramming have not only wide-spread relevance for brain injury and repair, but also highlight the urgency of improving the timely and coordinated metabolic conversion as well as protection from ferroptosis in aiming at neuronal repair.

EXPERIMENTAL PROCEDURE

Primary Cell Cultures

Astrocytes were cultured and transduced as described in Heinrich et al. (2010) and MEFs as described in Vierbuchen et al. (2010).

Live Imaging Microscopy

Time-lapse video microscopy was performed with a cell observer (Zeiss) at a constant temperature of 37°C and 8% CO₂. Phase contrast images were acquired every 5 minutes, and fluorescence pictures every 4-6 hours for 6.5-7.5 days using a 10x phase contrast objective (Zeiss), and an AxioCam HRm camera with a self-written VBA module remote controlling Zeiss AxioVision 4.7 software. Movies were assembled and analyzed using ImageJ (National Institute of Health, USA) software. For description of the analysis see supplementary procedures section.

Analysis of Lipid Peroxidation

For the detection of lipid peroxidation we used either the reagent Click-iT lipid peroxidation kit based on linoleamide alkyne (LAA) reagent (Life Technologies) or BODIPY® 581/591 C11 (C11-Bodipy, Molecular Probes; Drummen et al., 2002). Astroglial cells were first cultured and transfected as previously described (Heinrich et al., 2010; see also supplementary information). 3,5 days later the cells were labelled according to the specifications described in the product data sheet and fixed with 4% paraformaldehyde (PFA) for 5 minutes. Finally, the direct fluorescence of the reporters was detected by epi-fluorescent microscopy.

Animal Surgery

Operations were performed in accordance with the policies of the state of Bavaria under license number 55.2-1-54-2532-171-2011. Three days after performing a stab-wound injury (Sirko et al. 2013; Simon et al. 2011), 0.5-1 µl of retroviral suspension (*Neurog2-IRES-RFP* alone or 1:1 with *Bcl-2-IRES-GFP*) was injected into the site of the lesion as described by Heinrich et al., 2014. When indicated in the text, 200 µl of Calcitriol (1 ng/µl, Tocris) or αT3 (100 mg/kg body weight,

Sigma Aldrich) diluted in corn oil were administered through oral gavage at 2 DPI. The dosage was determined according with previous publications (Park et al., 2011; Nashold et al. 2013).

AUTHOR CONTRIBUTIONS

The authors have made the following declaration about their contributions: Conceived and designed the experiments: SG, MG. Designed in vivo experiments: SG, EM, MG. Performed in vivo experiments: EM. Performed in vitro experiments: SG, FO, AD, GLR, MK. Electrophysiological recordings: DP. Genome-wide experiments and analysis: MI, SG, MG, GM. Analyzed data: SG, EM, GM, FO, AD, GLR. Contributed reagents/materials/analysis tools: GM, MI, JB, JPFA, MC, CB, TS, SR. Wrote the paper: MG, SG, EM, BB. All authors discussed the manuscript.

ACKNOWLEDGEMENTS

We would like to thank Tatjana Ebert, Carmen Meyer, Detlef Franzen and Anke Pettenbrock for excellent technical assistance and Alex Lepier for advice with viral vector design. We are very grateful to Stefan Stricker, Leda Dimou and Sofia Grade for excellent comments on the manuscript. Anti-Prx-AK was a kind gift of C.H. Lillig (Ernst-Moritz-Arndt-University, Greifswald, Germany). This work was supported by the German Research Foundation to MG (GO 640/8-1, 10-1), the Helmholtz Portfolio Theme 'Metabolic Dysfunction and Common Disease' (JB) and the Helmholtz Alliance 'ICEMED' (JB, MG), the SFB 870 and the advanced ERC grant ChroNeuroRepair to MG as well as the grant "NewNeurons" to BB and MG financed by the Ministry of Science and Education and German Research Foundation Priority Program 'Pluripotency and Reprogramming' (BE 4182/2-2 and GO 640/9-2).

REFERENCES

- Abdul-Muneer, P.M., Chandra, N., and Haorah, J. (2014). Interactions of Oxidative Stress and Neurovascular Inflammation in the Pathogenesis of Traumatic Brain Injury. *Molecular neurobiology* 51(3):966-79
- Amamoto, R., and Arlotta, P. (2014). Development-inspired reprogramming of the mammalian central nervous system. *Science* 343, 1239882.

Anderova, M., Antonova, T., Petrik, D., Neprasova, H., Chvatal, A., and Sykova, E. (2004). Voltage-dependent potassium currents in hypertrophied rat astrocytes after a cortical stab wound. *Glia* 48, 311-326.

Arlotta, P., Molyneaux, B.J., Chen, J., Inoue, J., Kominami, R., and Macklis, J.D. (2005). Neuronal subtype-specific genes that control corticospinal motor neuron development in vivo. *Neuron* 45, 207-221.

Bao, B.Y., Ting, H.J., Hsu, J.W., and Lee, Y.F. (2008). Protective role of 1 alpha, 25-dihydroxyvitamin D3 against oxidative stress in nonmalignant human prostate epithelial cells. *International journal of cancer* 122, 2699-2706.

Berninger, B., Costa, M.R., Koch, U., Schroeder, T., Sutor, B., Grothe, B., and Gotz, M. (2007). Functional properties of neurons derived from in vitro reprogrammed postnatal astroglia. *The Journal of neuroscience* 27, 8654-8664.

Blum, R., Heinrich, C., Sanchez, R., Lepier, A., Gundelfinger, E.D., Berninger, B., and Gotz, M. (2011). Neuronal network formation from reprogrammed early postnatal rat cortical glial cells. *Cereb Cortex* 21, 413-424.

Buettner, G.R. (1993). The pecking order of free radicals and antioxidants: lipid peroxidation, alpha-tocopherol, and ascorbate. *Archives of biochemistry and biophysics* 300, 535-543.

Buffo, A., Vosko, M.R., Erturk, D., Hamann, G.F., Jucker, M., Rowitch, D., and Gotz, M. (2005). Expression pattern of the transcription factor Olig2 in response to brain injuries: implications for neuronal repair. *Proceedings of the National Academy of Sciences of the United States of America* 102, 18183-18188.

Chanda, S., Ang, C.E., Davila, J., Pak, C., Mall, M., Lee, Q.Y., Ahlenius, H., Jung, S.W., Sudhof, T.C., and Wernig, M. (2014). Generation of Induced Neuronal Cells by the Single Reprogramming Factor ASCL1. *Stem cell reports* 3, 282-296.

Degterev, A., Huang, Z., Boyce, M., Li, Y., Jagtap, P., Mizushima, N., Cuny, G.D., Mitchison, T.J., Moskowitz, M.A., and Yuan, J. (2005). Chemical inhibitor of nonapoptotic cell death with therapeutic potential for ischemic brain injury. *Nature chemical biology* 1, 112-119.

Deng, X., Gao, F., Flagg, T., Anderson, J., and May, W.S. (2006). Bcl2's flexible loop domain regulates p53 binding and survival. *Molecular and cellular biology* 26, 4421-4434.

Ding, N., Yu, R.T., Subramaniam, N., Sherman, M.H., Wilson, C., Rao, R., Leblanc, M., Coulter, S., He, M., Scott, C., *et al.* (2013). A vitamin D receptor/SMAD genomic circuit gates hepatic fibrotic response. *Cell* 153, 601-613.

Dixon, S.J., Lemberg, K.M., Lamprecht, M.R., Skouta, R., Zaitsev, E.M., Gleason, C.E., Patel, D.N., Bauer, A.J., Cantley, A.M., Yang, W.S., *et al.* (2012). Ferroptosis: an iron-dependent form of nonapoptotic cell death. *Cell* 149, 1060-1072.

Dong, J., Wong, S.L., Lau, C.W., Lee, H.K., Ng, C.F., Zhang, L., Yao, X., Chen, Z.Y., Vanhoutte, P.M., and Huang, Y. (2012). Calcitriol protects renovascular function in hypertension by down-regulating angiotensin II type 1 receptors and reducing oxidative stress. *European heart journal* 33, 2980-2990.

Drummen, G.P., van Liebergen, L.C., Op den Kamp, J.A., and Post, J.A. (2002). C11-BODIPY(581/591), an oxidation-sensitive fluorescent lipid peroxidation probe: (micro)spectroscopic characterization and validation of methodology. *Free radical biology & medicine* 33, 473-490.

Fode, C., Ma, Q., Casarosa, S., Ang, S.L., Anderson, D.J., and Guillemot, F. (2000). A role for neural determination genes in specifying the dorsoventral identity of telencephalic neurons. *Genes & development* 14, 67-80.

Friedmann Angeli, J.P., Schneider, M., Proneth, B., Tyurina, Y.Y., Tyurin, V.A., Hammond, V.J., Herbach, N., Aichler, M., Walch, A., Eggenhofer, E., *et al.* (2014). Inactivation of the ferroptosis regulator Gpx4 triggers acute renal failure in mice. *Nature cell biology* 16, 1180-1191.

George, N., Kumar, T.P., Antony, S., Jayanarayanan, S., and Paulose, C.S. (2012). Effect of vitamin D3 in reducing metabolic and oxidative stress in the liver of streptozotocin-induced diabetic rats. *The British journal of nutrition* 108, 1410-1418.

Gianforcaro, A., and Hamadeh, M.J. (2014). Vitamin D as a potential therapy in amyotrophic lateral sclerosis. *CNS neuroscience & therapeutics* 20, 101-111.

Godoy, J.R., Oesteritz, S., Hanschmann, E.M., Ockenga, W., Ackermann, W., and Lillig, C.H. (2011). Segment-specific overexpression of redoxins after renal ischemia and reperfusion: protective roles of glutaredoxin 2, peroxiredoxin 3, and peroxiredoxin 6. *Free radical biology & medicine* 51, 552-561.

Grande, A., Sumiyoshi, K., Lopez-Juarez, A., Howard, J., Sakthivel, B., Aronow, B., Campbell, K., and Nakafuku, M. (2013). Environmental impact on direct neuronal reprogramming in vivo in the adult brain. *Nature communications* 4, 2373.

Guo, Z., Zhang, L., Wu, Z., Chen, Y., Wang, F., and Chen, G. (2014). In vivo direct reprogramming of reactive glial cells into functional neurons after brain injury and in an Alzheimer's disease model. *Cell stem cell* 14, 188-202.

Halley-Stott, R.P., Jullien, J., Pasque, V., and Gurdon, J. (2014). Mitosis gives a brief window of opportunity for a change in gene transcription. *PLoS biology* 12, e1001914.

Heinrich, C., Bergami, M., Gascon, S., Lepier, A., Vigano, F., Dimou, L., Sutor, B., Berninger, B., and Gotz, M. (2014). Sox2-Mediated Conversion of NG2 Glia into Induced Neurons in the Injured Adult Cerebral Cortex. *Stem cell reports* 3, 1000-1014.

Heinrich, C., Blum, R., Gascon, S., Masserdotti, G., Tripathi, P., Sanchez, R., Tiedt, S., Schroeder, T., Gotz, M., and Berninger, B. (2010). Directing astroglia from the cerebral cortex into subtype specific functional neurons. *PLoS biology* 8, e1000373.

Imayoshi, I., and Kageyama, R. (2014). bHLH factors in self-renewal, multipotency, and fate choice of neural progenitor cells. *Neuron* 82, 9-23.

Jin, Z., May, W.S., Gao, F., Flagg, T., and Deng, X. (2006). Bcl2 suppresses DNA repair by enhancing c-Myc transcriptional activity. *The Journal of biological chemistry* 281, 14446-14456.

Kawamura, T., Suzuki, J., Wang, Y.V., Menendez, S., Morera, L.B., Raya, A., Wahl, G.M., and Izpisua Belmonte, J.C. (2009). Linking the p53 tumour suppressor pathway to somatic cell reprogramming. *Nature* 460, 1140-1144.

Kida, Y.S., Kawamura, T., Wei, Z., Sogo, T., Jacinto, S., Shigeno, A., Kushige, H., Yoshihara, E., Liddle, C., Ecker, J.R., *et al.* (2015). ERRs Mediate a Metabolic Switch Required for Somatic Cell Reprogramming to Pluripotency. *Cell stem cell* 16, 547-555.

Krishna, S., Low, I.C., and Pervaiz, S. (2011). Regulation of mitochondrial metabolism: yet another facet in the biology of the oncoprotein Bcl-2. *The Biochemical journal* 435, 545-551.

Kronenberg, G., Gertz, K., Cheung, G., Buffo, A., Kettenmann, H., Gotz, M., and Endres, M. (2010). Modulation of fate determinants Olig2 and Pax6 in resident glia evokes spiking neuroblasts in a model of mild brain ischemia. *Stroke* 41, 2944-2949.

Liu, M.L., Zang, T., Zou, Y., Chang, J.C., Gibson, J.R., Huber, K.M., and Zhang, C.L. (2013a). Small molecules enable neurogenin 2 to efficiently convert human fibroblasts into cholinergic neurons. *Nature communications* 4, 2183.

Liu, W., Long, Q., Chen, K., Li, S., Xiang, G., Chen, S., Liu, X., Li, Y., Yang, L., Dong, D., *et al.* (2013b). Mitochondrial metabolism transition cooperates with nuclear reprogramming during induced pluripotent stem cell generation. *Biochemical and biophysical research communications* 431, 767-771.

Maryanovich, M., and Gross, A. (2013). A ROS rheostat for cell fate regulation. *Trends in cell biology* 23, 129-134.

Masserdotti, G., Gillotin, S., Sutor, B., Drechsel, D., Irmeler, M., Jorgensen, H.F., Sass, S., Theis, F.J., Beckers, J., Berninger, B., *et al.* (2015). Transcriptional Mechanisms of Proneural Factors and REST in Regulating Neuronal Reprogramming of Astrocytes. *Cell stem cell* 17, 74-88.

McKay, N.D., Robinson, B., Brodie, R., and Rooke-Allen, N. (1983). Glucose transport and metabolism in cultured human skin fibroblasts. *Biochimica et biophysica acta* 762, 198-204.

Molyneaux, B.J., Arlotta, P., Menezes, J.R., and Macklis, J.D. (2007). Neuronal subtype specification in the cerebral cortex. *Nature reviews Neuroscience* 8, 427-437.

Nguyen, T., Nioi, P., and Pickett, C.B. (2009). The Nrf2-antioxidant response element signaling pathway and its activation by oxidative stress. *The Journal of biological chemistry* 284, 13291-13295.

Nieto, M., Monuki, E.S., Tang, H., Imitola, J., Haubst, N., Khoury, S.J., Cunningham, J., Gotz, M., and Walsh, C.A. (2004). Expression of Cux-1 and Cux-2 in the subventricular zone and upper layers II-IV of the cerebral cortex. *The Journal of comparative neurology* 479, 168-180.

Ninkovic, J., Steiner-Mezzadri, A., Jawerka, M., Akinci, U., Masserdotti, G., Petricca, S., Fischer, J., von Holst, A., Beckers, J., Lie, C.D., *et al.* (2013). The BAF complex interacts with Pax6 in adult neural progenitors to establish a neurogenic cross-regulatory transcriptional network. *Cell stem cell* 13, 403-418.

Niu, W., Zang, T., Zou, Y., Fang, S., Smith, D.K., Bachoo, R., and Zhang, C.L. (2013). In vivo reprogramming of astrocytes to neuroblasts in the adult brain. *Nature cell biology* 15, 1164-1175.

Park, S.K., Dahmer, M.K., and Quasney, M.W. (2012). MAPK and JAK-STAT signaling pathways are involved in the oxidative stress-induced decrease in expression of surfactant protein genes. *Cellular physiology and biochemistry* 30, 334-346.

Pearen, M.A., Eriksson, N.A., Fitzsimmons, R.L., Goode, J.M., Martel, N., Andrikopoulos, S., and Muscat, G.E. (2012). The nuclear receptor, Nor-1, markedly increases type II oxidative muscle fibers and resistance to fatigue. *Mol Endocrinol* 26, 372-384.

Pedroni, A., Minh do, D., Mallamaci, A., and Cherubini, E. (2014). Electrophysiological characterization of granule cells in the dentate gyrus immediately after birth. *Frontiers in cellular neuroscience* 8, 44.

Prozorovski, T., Schneider, R., Berndt, C., Hartung, H.P., and Aktas, O. (2015). Redox-regulated fate of neural stem progenitor cells. *Biochimica et biophysica acta* 1850, 1543-1554.

Qi, S., Fang, Z., Wang, D., Menendez, P., Yao, K., and Ji, J. (2015). Concise review: induced pluripotency by defined factors: prey of oxidative stress. *Stem Cells* 33, 1371-1376.

Ruiz, S., Panopoulos, A.D., Herrerias, A., Bissig, K.D., Lutz, M., Berggren, W.T., Verma, I.M., and Izpisua Belmonte, J.C. (2011). A high proliferation rate is required for cell reprogramming and maintenance of human embryonic stem cell identity. *Current biology* 21, 45-52.

Schuurmans, C., Armant, O., Nieto, M., Stenman, J.M., Britz, O., Klenin, N., Brown, C., Langevin, L.M., Seibt, J., Tang, H., *et al.* (2004). Sequential phases of cortical specification involve Neurogenin-dependent and -independent pathways. *The EMBO journal* 23, 2892-2902.

Sherman, M.H., Yu, R.T., Engle, D.D., Ding, N., Atkins, A.R., Tiriach, H., Collisson, E.A., Connor, F., Van Dyke, T., Kozlov, S., *et al.* (2014). Vitamin d receptor-mediated stromal reprogramming suppresses pancreatitis and enhances pancreatic cancer therapy. *Cell* 159, 80-93.

Theofilopoulos, S., Wang, Y., Kitambi, S.S., Sacchetti, P., Sousa, K.M., Bodin, K., Kirk, J., Salto, C., Gustafsson, M., Toledo, E.M., *et al.* (2013). Brain endogenous liver X receptor ligands selectively promote midbrain neurogenesis. *Nature chemical biology* 9, 126-133.

Torper, O., Pfisterer, U., Wolf, D.A., Pereira, M., Lau, S., Jakobsson, J., Bjorklund, A., Grealish, S., and Parmar, M. (2013). Generation of induced neurons via direct conversion in vivo. *Proceedings of the National Academy of Sciences of the United States of America* 110, 7038-7043.

Tsacopoulos, M., and Magistretti, P.J. (1996). Metabolic coupling between glia and neurons. *The Journal of neuroscience : the official journal of the Society for Neuroscience* 16, 877-885.

Wapinski, O.L., Vierbuchen, T., Qu, K., Lee, Q.Y., Chanda, S., Fuentes, D.R., Giresi, P.G., Ng, Y.H., Marro, S., Neff, N.F., *et al.* (2013). Hierarchical mechanisms for direct reprogramming of fibroblasts to neurons. *Cell* 155, 621-635.

Yang, W.S., SriRamaratnam, R., Welsch, M.E., Shimada, K., Skouta, R., Viswanathan, V.S., Cheah, J.H., Clemons, P.A., Shamji, A.F., Clish, C.B., *et al.* (2014). Regulation of ferroptotic cancer cell death by GPX4. *Cell* 156, 317-331.

Yin, X.M., Oltvai, Z.N., and Korsmeyer, S.J. (1994). BH1 and BH2 domains of Bcl-2 are required for inhibition of apoptosis and heterodimerization with Bax. *Nature* 369, 321-323.

Zhang, J., Nuebel, E., Daley, G.Q., Koehler, C.M., and Teitell, M.A. (2012). Metabolic regulation in pluripotent stem cells during reprogramming and self-renewal. *Cell stem cell* 11, 589-595.

FIGURE LEGENDS

Figure 1. Time-lapse Analysis of Astrocyte-to-Neuron Reprogramming.

(A) Schematic of the experimental protocol used for time-lapse video analysis.

(B) Still images from video-time lapse movies (see Movie S1) showing cells classified as non-neuronal/astroglial (green arrows), neuronal (yellow arrows) and dying (red arrows) at the time *in vitro* indicated transfected with the constructs indicated.

(C) Progeny-trees of single cells tracked from example in B showing astrocytes (green lines) dead cells (depicted with “x”) and neurons (yellow lines).

(D-H) Histograms depicting cell survival and neuronal conversion from movies (N=5 for control; 339 cells tracked; N=4 with Bcl-2, 237 cells tracked) based on morphological classification as detailed and verified by immunostaining in Figure S1A-D. The percentage of neurons is normalized to the initial number of transfected cells in D, E.

(I) Schematic summary of reprogramming and cell death as indicated by gradients of the respective colour.

Error bars indicate \pm SD. ** $p < 0.01$, *** $p < 0.001$, $p \geq 0.05$ no statistically significant difference (n.s.); ANOVA Tukey’s post-hoc test in D; t test in E, F, G, H. Scale bars 40 μ m.

See also Figure S1 and Movies S1/S2.

Figure 2. Non-canonical, BAX-independent Effect of Bcl-2 on Neuronal Reprogramming.

(A) Cartoon depicting previously described interactions of Bcl-2 with several molecular partners as described in the text.

(B, C) Histograms (with corresponding micrographs showing immunostaining for β -III-tubulin, in D) depicting the survival and fate conversion rate at 5DPT (for details see supplementary material) in astroglial cultures transfected with the constructs indicated (N=3; cells=900-2500 for each condition).

(E, I) Histograms showing the proportion of β -III-tubulin+ neurons at 7 days after transduction of astrocytes with a viral vector containing Neurog2 alone or with Bcl-2 (E, N=3; cells=1500-2000 for each condition) or 15 DPI of MEFs with the vector indicated (I, N=3; Cells=340-700 for each condition).

(F) Confocal micrographs showing that iNs from E are immuno-reactive for vGluT1 at 15 DPI.

(G) Arrows indicate astrocytes co-transfected with Bcl-2 and RFP (Red cells) being immuno-positive for GFAP (green) and retaining astroglial morphology at 7 DPT.

(H) Micrographs of fibroblast conversion into neurons (β -III-tubulin+ cells; green) at 15 DPI upon transduction with retroviral vectors of the constructs indicated.

Error bars indicate \pm SD. * p <0.05, ** p <0.01, *** p <0.001; ANOVA with Tukey's post-hoc test in B, C, I; t test in E. Scale bars: 50 μ m in D, H; 10 μ m in F.

See also Figure S2.

Figure 3. Ferroptosis and Lipid Peroxidation Are Key Limiting Factors During Neuronal Reprogramming.

(A, B, D) Histograms showing the percentage of survival and iNs (A, B) or Lipid ROS+ cells (D, N=3, for RFP, Bcl-2, A(70)-Bcl-2, α Toc; N=4 for EE-Bcl-2 and Ascl1; cells=80-500 each condition) in astroglial cultures treated as indicated on the X-axis. Treatment with ZVAD (20 μ g/ μ l), Necrostatin (10 μ M) or Liproxstatin-1 (200 nM) was performed at 1DPT (N=4, A,B; cells=1500-2000).

(C, E) Confocal micrographs of Lip-Ox (Life Technologies, green reporter) staining (C, treatment with cumene hydroperoxide 100 μ M; positive control for Lip-Ox, or α Toc 10 μ M; negative control for Lip-Ox, at 1DPT) or C11-Bodipy (E) in astrocytes transfected as indicated at 3.5 DPT. Arrows indicate transfected cells (red) with increased levels of Lip-Ox (green); arrowheads transfected cells without green signal.

Error bars indicate \pm SD. * p <0.05, ** p <0.01, *** p <0.001; ANOVA with Tukey's post-hoc test in B, D; ANOVA with Dunnett's post-hoc test in A. Scale bars 40 μ m.

See also Figure S3.

Figure 4. Increased Reprogramming Mediated by a Reduction of Lipid Peroxidation Levels is Reproduced by Treatment with Forskolin.

(A, B) Histograms show iNs (β -III-tubulin+; green in micrographs in C) and survival rate at 5 DPT from astroglial cells transfected and treated as detailed in Figure 3 (N=3; cells=1500-2000).

(D, E) Micrographs (D) and histogram (E, N=3; cells=110-200) of survival rate/neuronal conversion of astroglia transfected with *Ascl1/RFP* (red cells) and cultured 5 days in absence/presence of 10 μ M Fk. Neuronal conversion was monitored by β -III-tubulin (green).

(F, H) Micrographs showing examples of the C11-Bodipy reporter (F) or CellROX reporter (green in H) in astrocyte cultures transfected and treated as indicated at 3.5 DPT. Arrows depict transfected cells (red) with increased levels of ROS (green); empty arrows depict untransfected cells; arrowheads show transfected cells with low ROS signal.

(G) Quantification of cells depicted in F. The result with α Toc treatment has been included to compare with the effect of Fk (N=3 for α Toc; N=4 in *Ascl1* and *Ascl1*+Fk; cells=80-250).

(I) Immunoblots showing that 24 h-treatment with Fk reduces the levels of oxidized Prx2 (dimer, upper band) in both astroglial cultures (upper panel) and MEFs (lower panel) infected with *Ascl1/RFP*-encoding vectors.

Error bars indicate \pm SD. * p <0.05, ** p <0.01, *** p <0.001; ANOVA with Dunnett's post-hoc test in A, B, E; ANOVA with Tukey's post-hoc test in G. Scale bars 40 μ m in C and D; 20 μ m in F and 80 μ m in H.

See also Figure S4 and Movie S3.

Figure 5. Transcriptome and Functional Analysis of Genes Activated by Fk and Bcl-2.

(A) Schematic drawing of the experimental protocol.

(B) Heatmaps of linear fold changes with the top 60 up-regulated genes (left) or transcriptional regulators (right) in microarrays of *Ascl1*+Fk vs *Ascl1* only transduced MEFs; $p<0.01$, fold-change ≥ 1.5 .

(C) Histogram showing qRT-PCR for genes predicted to be regulated by the microarray analysis (ratio paired t test, $p<0.01$; FC ≥ 1.5). Genes with lower significance were also validated ($p<0.07$; shown in red).

(D) Bars represent fold change of luciferase levels from a Nrf2-responsive construct co-transfected with *Ascl1* in astroglial cultures induced by Fk (15, 24 and 48 h) compared to untreated cells.

(E) qRT-PCR analysis of mRNA levels from 4 representative targets induced by Fk in MEFs and astrocytes.

(F) Western Blot depicting levels of Vdr protein after 24 h treatment with Fk in astroglia cultures infected with *RFP*- or *Ascl1/RFP*-encoding retroviral vectors.

(G) Percentage of astrocytes positive for the lipid reporter based on linoleic acid (Life Technologies) among the *Ascl1*- or *Ascl1+Vdr*-transfected population at 3.5 DPT. N=3

(H,I) Histograms and corresponding micrographs (J,K) depicting the neuronal conversion efficiency of astroglial cultures transfected with constructs indicated on X axis at 5 DPT (N=3; cells=80-250).

* $p<0.05$, ** $p<0.01$, *** $p<0.001$, **** $p<0.0001$; ratio paired t test in (C); two-way ANOVA with Sidak's post-hoc test in D; t test in (G); ANOVA with Tukey's post-hoc test in G, H; ANOVA with Dunnett's comparison test in I. Scale bars: 40 μm .

See also Figure S5 and Tables S1/S2/S3/S4.

Figure 6. Conversion of Reactive Glia Into Neurons Is Improved by *Bcl-2*, Calcitriol and α -Tocotrienol *In Vivo*.

(A) Scheme of the protocol used for stab-wound injury and subsequent infection with retroviral vectors for *Neurog2*-IRES-*RFP* and *Bcl-2*-IRES-*GFP*, the respective treatments and analysis time points.

(B) High-power micrograph of cells infected by *Neurog2-IRES-RFP* alone or with *Bcl-2-IRES-GFP* stained for NeuN at 10 days post infection (DPI), with orthogonal projections of the confocal stack. The RFP+ cell maintains an astroglial morphology and is NeuN-immunonegative (arrows, left panels), whereas the co-infected cell displays a distinct neuronal-like morphology and NeuN signal (right panels).

(C-E) Confocal micrographs of the injection site at 10 DPI upon the treatments indicated (C, none; D, Calcitriol; E, α T3) stained for NeuN. Co-infected cells immunopositive for NeuN (arrowheads) are shown at higher magnification in single optical sections (*, **, ***; right panels).

(F) Histogram with the proportion of induced, NeuN+ neurons amongst RFP+ and RFP+/GFP+ cells at 10 DPI, without (N=3) or with treatments (calcitriol, N=3; α T3, N=4).

(G, H) Micrographs of maximum intensity projections of neuronal examples as indicated. Inserts show single optical section of the NeuN+ nucleus (*; white arrow). The blue and red boxes in H (**, ***) display higher magnifications of a process with spine-like structures.

Error bars indicate \pm SD. * p <0.05, ** p <0.01, **** p <0.0001; two-way ANOVA with Tukey's post-hoc test in F. Scale bars: 10 μ m, except 20 μ m in B.

See also Figure S6.

Figure 7. Subtype Identity of Induced Neurons After Stab-wound Injury.

(A, B) Confocal micrographs (maximum intensity projection, A) and histogram of soma size (B) of cells at 10 days post infection by *Neurog2/RFP* and *Bcl-2/GFP* retroviral vectors after stab-wound injury and α T3 treatment (see Figure 6A) with thick processes and spine-like structures (box X, left panel). The soma size of these cells (NeuN staining, magnified in boxes *, **, ***; arrowheads) is similar to the size of nearby endogenous neurons (arrows), unlike for mice that did not receive α T3 (right panel, magnified in ****).

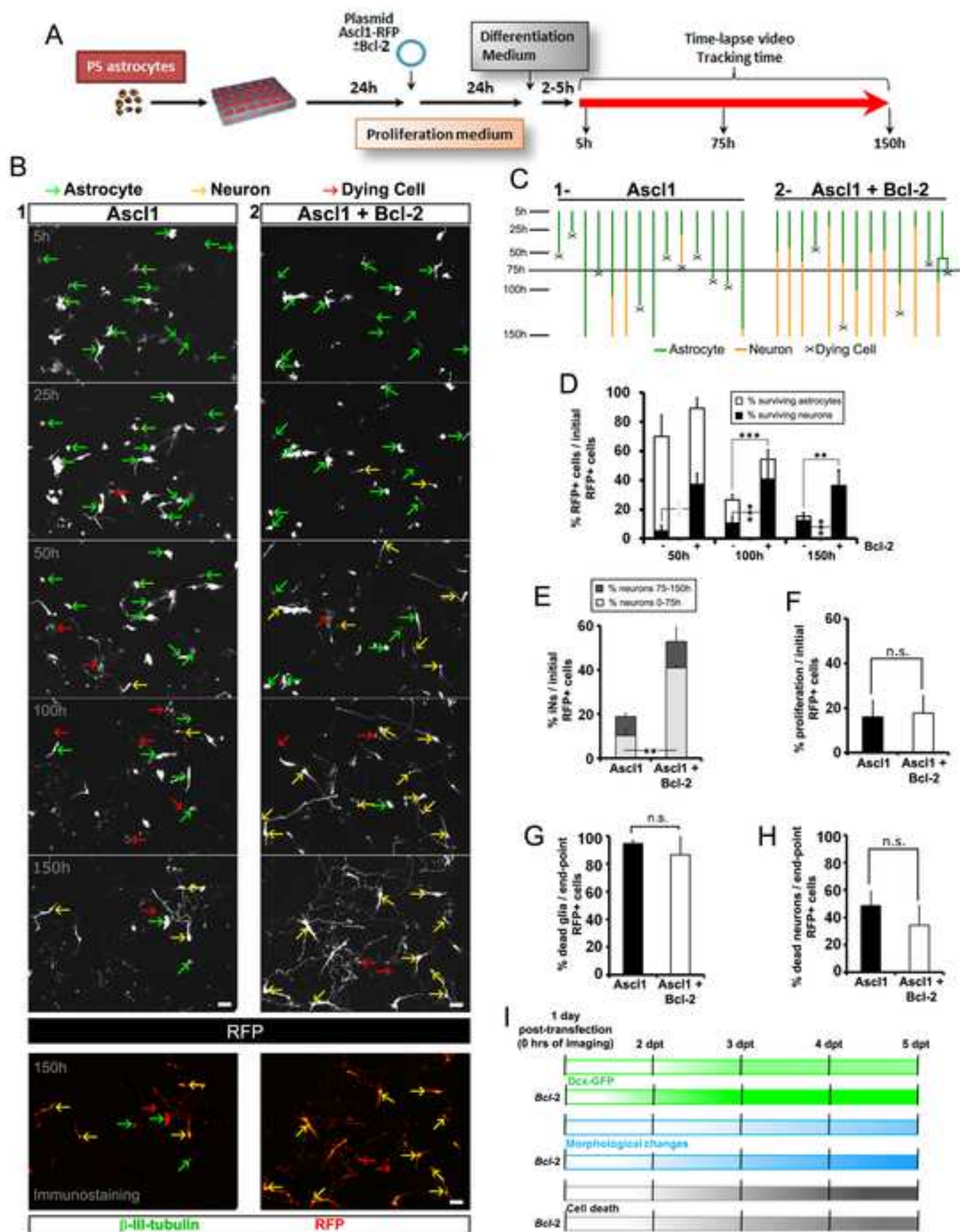
(C-F) Confocal micrographs showing neuronal subtype markers FoxP2 (C), Ctip2 (D), GABA (E), Satb2 and Cux1 (F) at 10 DPI. Filled arrowheads indicate immunopositive, empty arrowheads

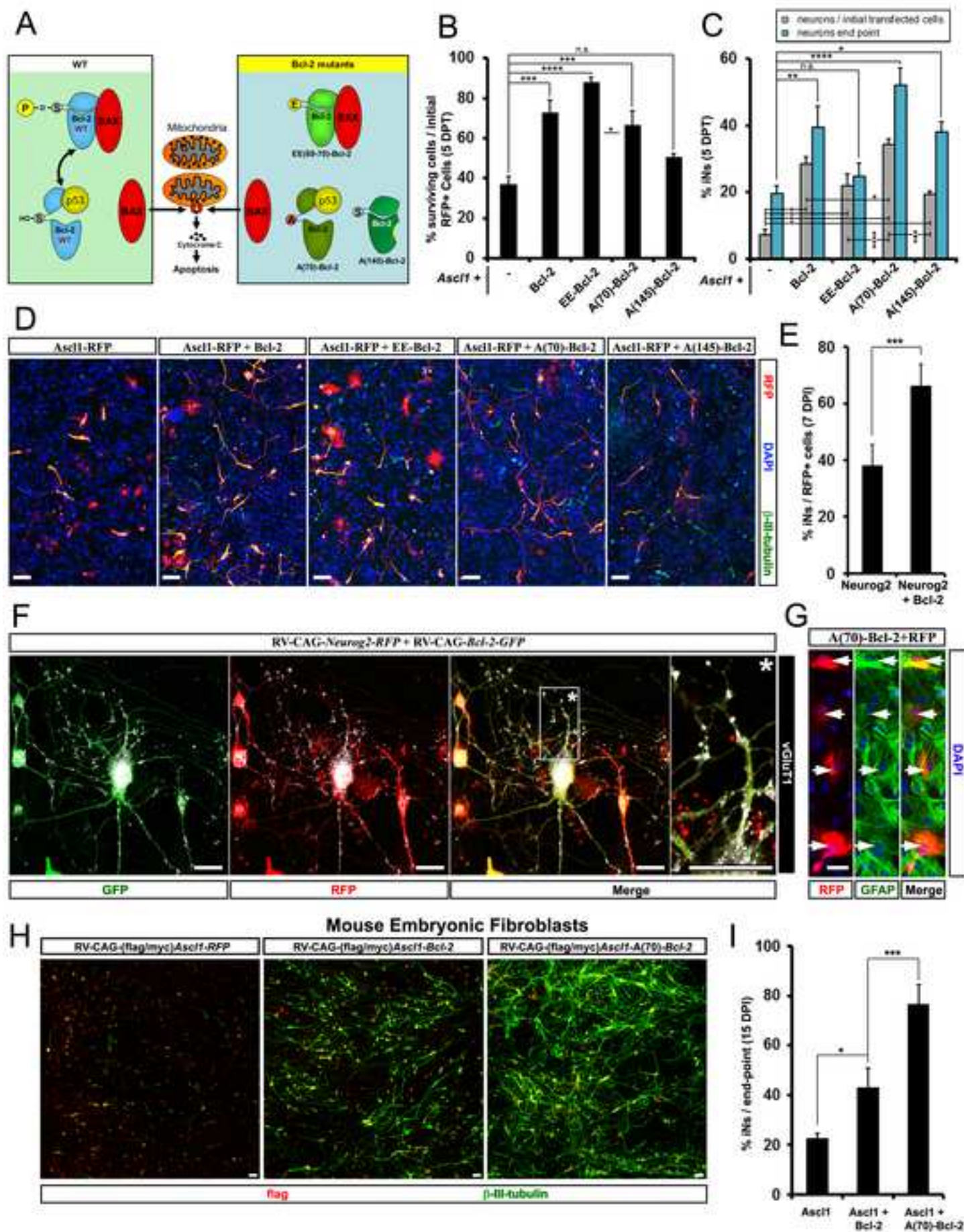
immunonegative cells in the squared box (*,**). Specific examples of cells located in upper or deep layers are depicted in F.

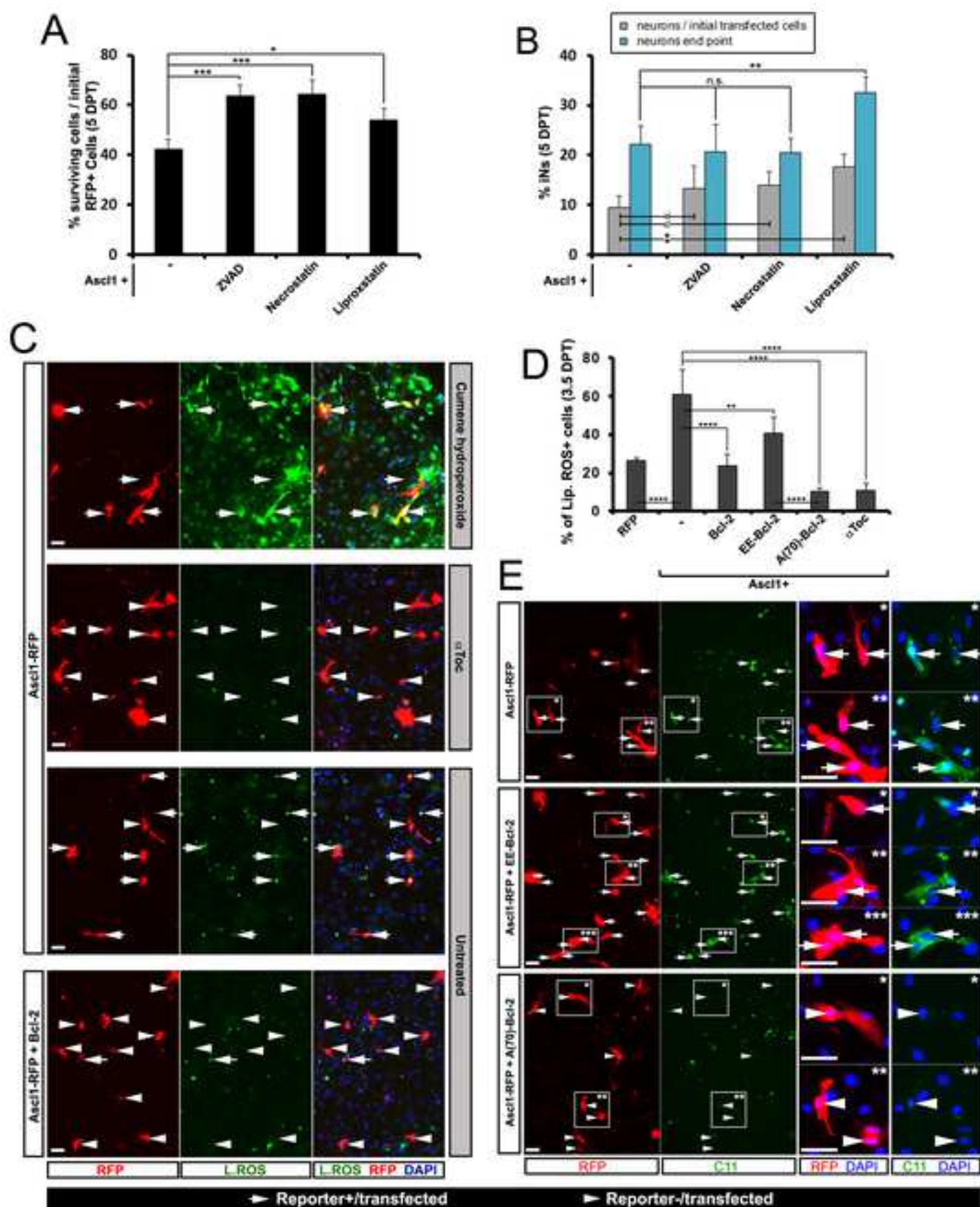
(G) Histogram of double infected cells expressing the indicated markers.

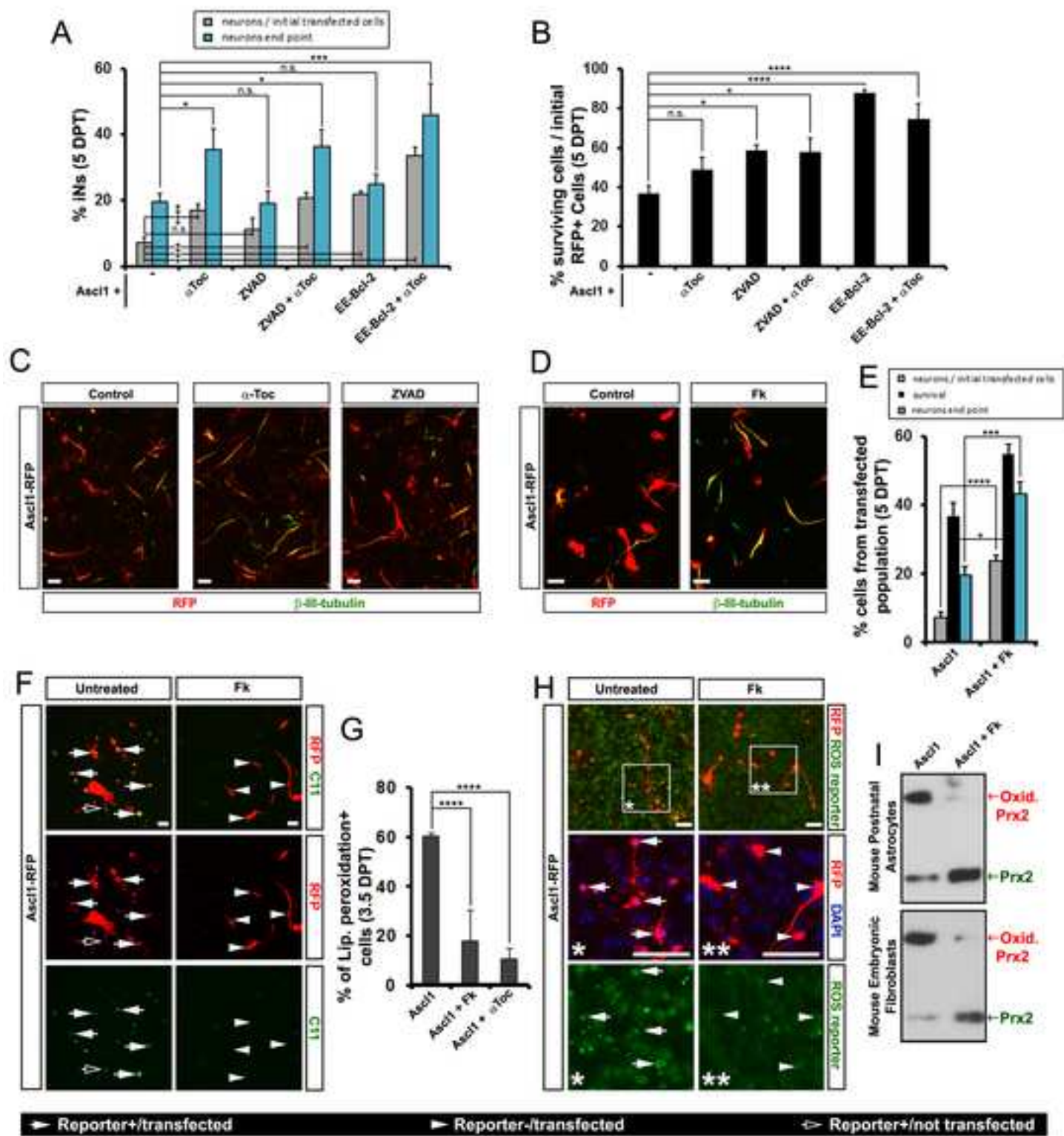
Horizontal lines in B indicate the mean. N=4 in A and B (α T3); N=3 in B (no treatment and calcitriol), C, D and G for Ctip2 and FoxP2; N=2 in E, F and G for Cux1 and Satb2. * $p < 0.05$; one-way ANOVA with Tukey's post-hoc test in B. Scale bars: 10 μ m.

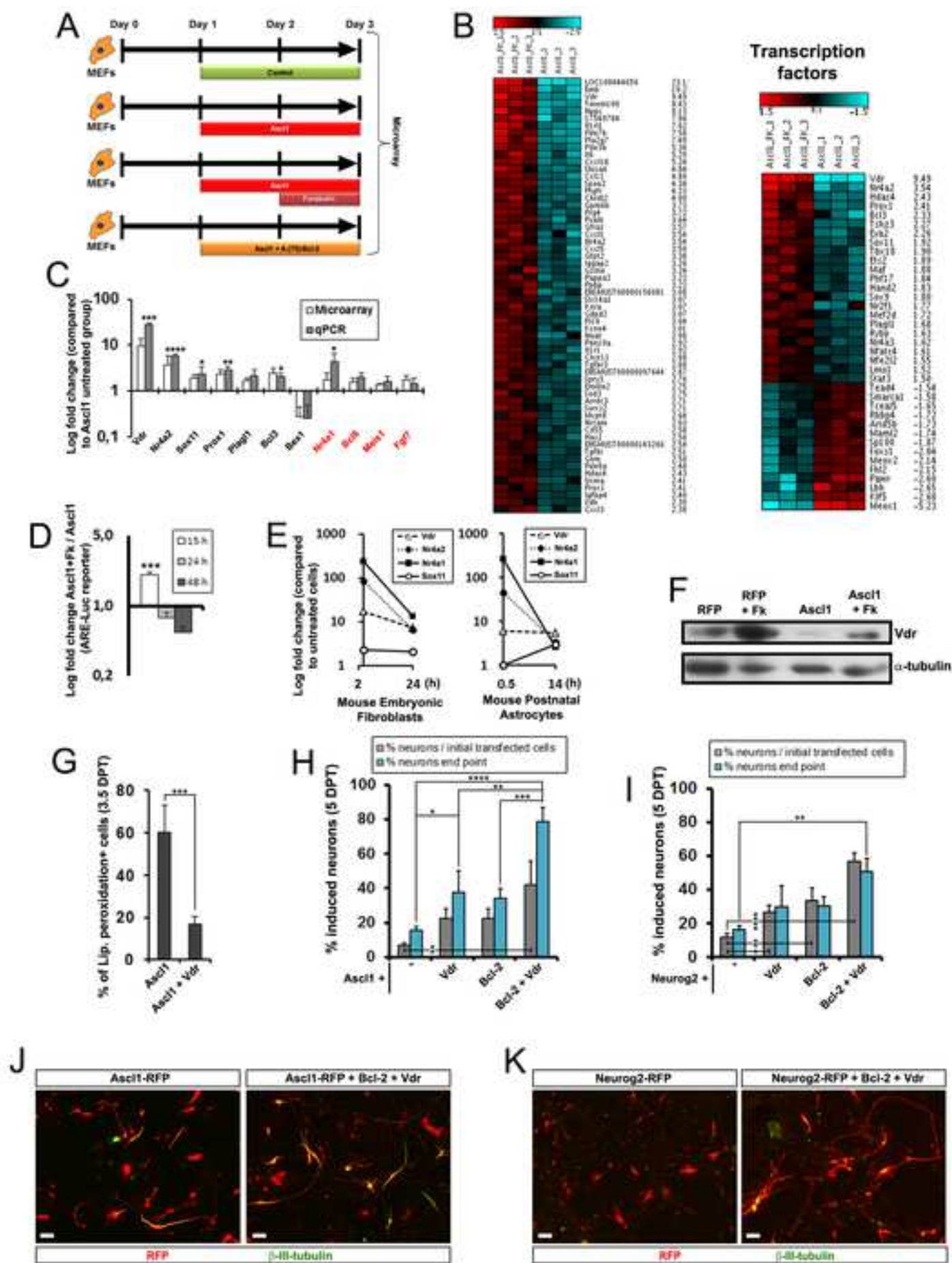
See also Figure S7.

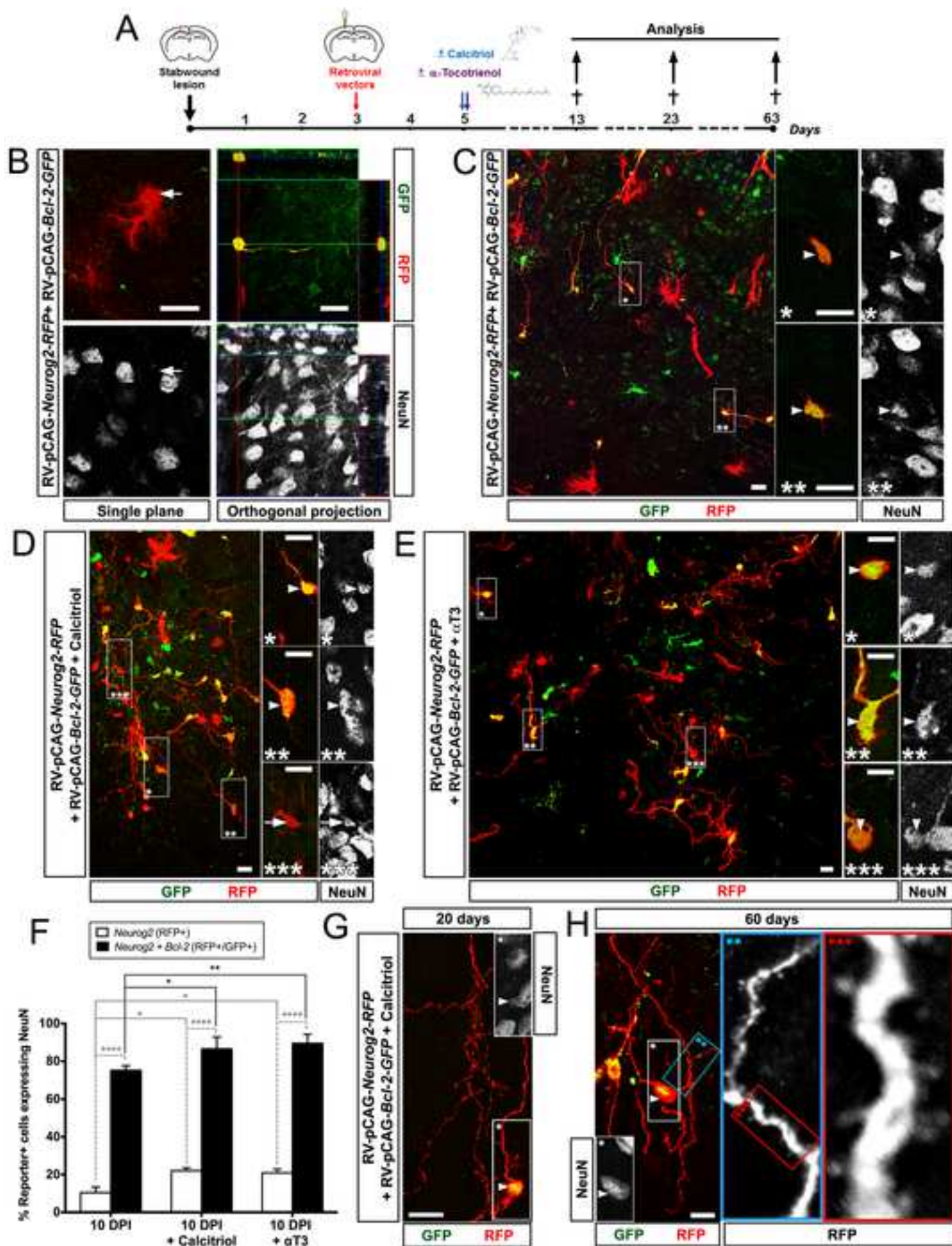












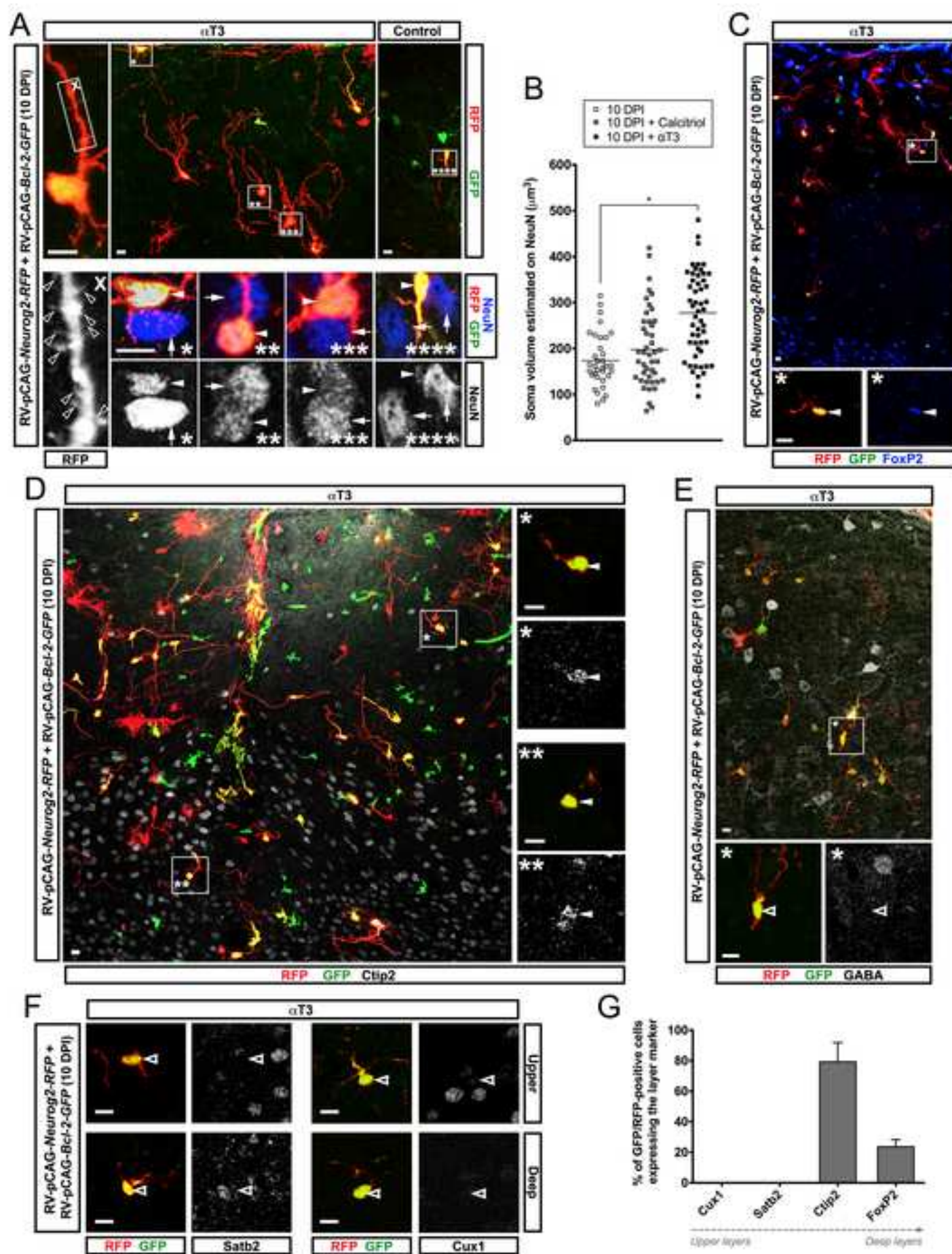


Table S1

Symbol or ID	Probeset	rawp	FC \geq 1.5x, p<0.01, Av>20 (507)
Ren1	17217335	0.00007	23.11
Emb	17290083	7.0E-07	10.21
Vdr	17321078	0.00003	9.49
Tmem100	17255058	1.5E-07	8.63
Nppc	17225191	0.00021	8.13
Emb	17549784	0.00002	7.96
Il1rl1	17212211	0.00014	7.62
Pde7b	17239638	0.00001	7.58
Pla2g7	17337796	0.00001	7.49
Pde3b	17482021	2.9E-06	5.36
Il6	17435725	0.00022	5.29
Cxcl14	17293006	1.9E-06	5.24
Shisa6	17264282	0.00089	4.84
Ccl11	17254053	0.00001	4.80
Spon2	17447081	1.1E-07	4.34
Ptgfr	17411163	0.00001	4.23
Chrdl2	17480620	0.00081	4.00
Gpm6b	17539611	0.00003	3.73
Prg4	17227892	0.00004	3.72
Pvalb	17318942	0.00007	3.64
Gfra1	17365960	0.00012	3.57
Cxcl1	17438987	0.00394	3.54
Nr4a2	17385374	0.00037	3.54
Cxcl5	17438955	0.00043	3.50
Gfpt2	17249036	0.00025	3.38
lqgap2	17295136	0.00014	3.26
Gzmd	17306983	0.00756	3.24
Pappa2	17228667	0.00010	3.23
Ppbp	17438963	0.00010	3.22
Gm12840	17417699	0.00132	3.08
Slc14a1	17355565	0.00006	3.07
Kera	17236816	0.00085	3.07
Gdpd2	17536600	0.00005	3.07
Pi16	17335506	0.00030	3.04
Kcne4	17214711	0.00121	3.01
Nnat	17393764	0.00190	2.98
Pde10a	17333133	0.00014	2.92
Il1r1	17212185	0.00034	2.92
Chst11	17235941	0.00054	2.88
Tgfbr3	17450618	0.00046	2.88
Hdac4	17225531	0.00046	2.87
Spry3	17546246	0.00039	2.76
Emilin2	17346975	0.00003	2.75
Sod3	17437385	0.00230	2.75
Arrdc3	17288876	0.00007	2.71
Sorcs2	17447404	0.00623	2.71
Mcpt8	17306968	0.00729	2.64

Nrcam	17275255	0.00001	2.63
Cd55	17226622	0.00029	2.58
Has2	17317167	0.00053	2.56
Gm15675	17226618	0.00004	2.54
Tgfb1	17287827	0.00003	2.51
Gem	17411840	0.00137	2.50
Pde8a	17479668	0.00003	2.48
Hdac4	17225535	0.00004	2.43
Ucma	17366525	0.00714	2.41
Prox1	17230960	0.00057	2.41
Igfbp4	17256264	0.00003	2.40
Xdh	17347163	0.00280	2.39
Cxcl3	17438975	0.00995	2.38
Mt2	17503937	0.00107	2.36
Rnf122	17500391	0.00592	2.34
Bcl3	17487457	0.00400	2.33
Ppap2b	17416234	0.00046	2.30
Slpi	17394153	0.00038	2.30
Pde1a	17387276	0.00026	2.29
Prl8a8	17291430	0.00035	2.29
Tshz3	17476866	0.00006	2.27
Il33	17358598	0.00342	2.27
Stac2	17268714	0.00075	2.26
Eya2	17379692	0.00074	2.26
Syt4	17548044	0.00999	2.26
Dio2	17282970	0.00234	2.26
Sik1	17343263	0.00058	2.25
Bmper	17515478	0.00006	2.25
Sv2b	17492220	0.00094	2.25
Pitpnc1	17271118	0.00327	2.24
Rspo1	17418403	0.00202	2.23
Gm16277	17360728	0.00857	2.23
Ppp1r3c	17364208	0.00102	2.21
Adam12	17497246	0.00006	2.20
Timp1	17533713	0.00025	2.19
Slc1a3	17315860	0.00036	2.19
Tnfaip6	17370735	0.00220	2.18
Bace2	17327544	0.00146	2.16
17291193	17291193	0.00374	2.16
Myo7a	17493467	0.00029	2.15
Angptl4	17343628	0.00704	2.15
Ndnf	17459207	0.00033	2.14
Crabp2	17398895	0.00015	2.11
ENSMUST0000C	17353239	0.00612	2.11
Tubb3	17506631	0.00522	2.10
Cd24a	17240606	0.00076	2.10
Tes	17548534	0.00001	2.09
Gdf10	17298731	0.00298	2.09
Srgap1	17245539	0.00116	2.08
Errfi1	17421972	0.00004	2.07

Slco2a1	17520905	0.00139	2.06
Slc16a2	17543817	0.00039	2.06
Dusp10	17220475	0.00030	2.04
Fbln1	17313811	0.00079	2.04
Pde3a	17464040	0.00256	2.02
Slc16a1	17401335	0.00057	2.01
Csrp2	17237208	0.00126	2.01
LOC100038987	17366314	0.00994	2.00
Tspan11	17463387	0.00203	1.99
Dpt	17218927	0.00253	1.98
Sfrp1	17500068	0.00141	1.97
Gm23320	17535987	0.00454	1.97
Cdh6	17316120	0.00008	1.96
Cables1	17348435	0.00076	1.96
Tnfsf11	17308817	0.00072	1.95
Ank3	17234066	0.00198	1.95
Aff2	17535245	0.00089	1.94
Ralgds	17368685	0.00169	1.94
Tnfrsf23	17498323	0.00098	1.93
Sned1	17215932	0.00127	1.93
Sox11	17280350	0.00020	1.92
Mgst1	17463909	0.00035	1.90
Plekhg1	17231366	0.00152	1.90
Gm20186	17456281	0.00017	1.90
Tes	17456131	0.00081	1.90
Tbx18	17529481	0.00139	1.90
Nap1l5	17467205	0.00598	1.90
S1pr3	17287325	0.00098	1.89
Ets2	17327465	0.00122	1.89
Slit3	17248426	0.00439	1.89
Maf	17513289	0.00361	1.88
Lrig1	17469217	0.00109	1.88
Pde4b	17416023	0.00044	1.87
Kif26b	17219997	0.00096	1.87
Hsph1	17455507	0.00305	1.86
BC028471	17444970	0.00189	1.86
Pde8b	17295059	0.00377	1.85
Socs3	17547600	0.00676	1.85
Pdgfra	17438246	0.00421	1.84
Phf17	17397344	0.00551	1.84
Gm10007	17360731	0.00267	1.84
Agtr1a	17286271	0.00601	1.84
Tiparp	17548270	0.00424	1.83
Hand2	17501272	0.00161	1.83
Mmp12	17514495	0.00590	1.83
A130040M12Ri	17267418	0.00522	1.83
ENSMUST0000C	17448166	0.00187	1.82
Slc10a6	17450319	0.00276	1.81
Rassf2	17391920	0.00495	1.81
Mt1	17503942	0.00168	1.81

Galnt2	17506732	0.00487	1.81
Cdkn1c	17498245	0.00031	1.81
Enpep	17410251	0.00320	1.81
Kcnd2	17456308	0.00177	1.80
Hgf	17434933	0.00039	1.80
Sox9	17257946	0.00813	1.80
Plxna2	17220974	0.00153	1.78
Cpa4	17456886	0.00213	1.78
Scgb1c1	17484610	0.00030	1.77
Nr2f1	17294547	0.00743	1.77
Ptchd1	17545618	0.00008	1.77
Pde1c	17467072	0.00211	1.76
Tmem178b	17457550	0.00181	1.76
Plat	17499962	0.00276	1.76
Ier5l	17383663	0.00484	1.76
Gclm	17402283	0.00409	1.76
Edil3	17288992	0.00039	1.76
Gdf6	17411727	0.00129	1.76
Wnt4	17420154	0.00348	1.75
9330133O14Rik	17506398	0.00053	1.74
Cdh4	17380659	0.00119	1.73
Kitl	17236900	0.00197	1.73
Acsl4	17545051	0.00064	1.73
Adcy2	17294086	0.00009	1.72
Mef2d	17398970	0.00364	1.72
ENSMUST0000C	17232438	0.00769	1.71
Agtr2	17533746	0.00271	1.70
Pappa	17414802	0.00147	1.70
Zfp930	17501672	0.00918	1.69
Htr3a	17526717	0.00025	1.69
Lpar1	17425686	0.00038	1.68
Gchfr	17374738	0.00178	1.68
Gpr137b	17290695	0.00843	1.68
B3galt1	17371310	0.00161	1.68
Ier3	17337228	0.00882	1.68
Abca1	17425301	0.00588	1.68
Gprc5b	17495610	0.00017	1.68
Plagl1	17231694	0.00033	1.68
Atp1b1	17229178	0.00077	1.67
Acvr1b	17315152	0.00705	1.67
Ptk7	17345475	0.00363	1.67
Pkdcc	17339973	0.00334	1.66
Calca	17495328	0.00008	1.66
Angpt1	17316780	0.00275	1.65
Steap1	17445440	0.00043	1.65
Gdf5	17393390	0.00054	1.65
Slc16a3	17259534	0.00965	1.64
Clstn2	17529930	0.00132	1.64
Rybp	17469463	0.00665	1.63
Il1rl2	17212199	0.00579	1.63

Fzd1	17445325	0.00261	1.63
Car13	17396143	0.00015	1.63
1810022K09Rik	17404174	0.00717	1.63
LOC101056010	17227379	0.00939	1.62
2300009N04Rik	17330625	0.00811	1.62
Nr4a3	17413945	0.00537	1.62
Tmem189	17394727	0.00961	1.61
Nfatc4	17300672	0.00081	1.61
Gdpd1	17267430	0.00071	1.61
Vipr2	17279562	0.00473	1.61
Tm7sf2	17361921	0.00734	1.60
Lypd1	17226435	0.00636	1.60
Ecm1	17407850	0.00392	1.60
Olfr311	17250115	0.00251	1.60
Apbb1ip	17367536	0.00234	1.60
Kremen1	17260137	0.00371	1.60
Gdf11	17246352	0.00952	1.60
Syt13	17373530	0.00738	1.60
Thpo	17329195	0.00629	1.60
Epb4.1l3	17339313	0.00046	1.59
Enpp1	17239787	0.00084	1.59
Has1	17341269	0.00384	1.59
Tiparp	17398082	0.00298	1.58
Cntfr	17424279	0.00939	1.58
AI593442	17527027	0.00355	1.58
Sdk2	17271632	0.00279	1.58
Il4ra	17482943	0.00446	1.58
Add3	17360312	0.00200	1.57
Clmp	17516352	0.00048	1.57
Slc6a17	17409005	0.00168	1.56
Sbsn	17476528	0.00042	1.56
Irak3	17245399	0.00240	1.56
Kif21a	17320614	0.00077	1.56
Nod1	17467015	0.00708	1.55
Nfe2l2	17386700	0.00364	1.55
ENSMUST0000C	17221434	0.00927	1.54
Gm5595	17490078	0.00153	1.54
Hs3st1	17447726	0.00334	1.54
Atp8b1	17355026	0.00620	1.54
Lrrc32	17480485	0.00636	1.53
Arl4c	17225360	0.00060	1.53
Rhou	17506697	0.00060	1.53
S100a14	17399776	0.00639	1.53
Cntn1	17314387	0.00506	1.53
Osmr	17315743	0.00572	1.53
Mpi	17527532	0.00726	1.53
LOC100862618	17258023	0.00144	1.53
Steap2	17445426	0.00221	1.52
Zfp503	17303989	0.00175	1.52
Ypel4	17372592	0.00051	1.52

Cirbp	17235227	0.00882	1.52
Lmo1	17494842	0.00172	1.52
Gna14	17357971	0.00421	1.51
Dclk1	17397708	0.00439	1.51
Flywch2	17341619	0.00372	1.51
Gm16564	17230301	0.00055	1.51
Cpt1a	17355915	0.00760	1.51
Mthfd2l	17439003	0.00432	1.50
U90926	17449649	0.00881	1.50
Slc4a7	17297227	0.00137	1.50
Stat3	17269717	0.00458	1.50
4931406H21Rik	17297748	0.00508	1.50
Tsnax	17506854	0.00676	1.50
Krt5	17321966	0.00042	1.50
Usp2	17516469	0.00457	1.50
Gm3696	17303088	0.00667	-1.50
Ablim1	17365911	0.00307	-1.50
Myo1c	17253055	0.00320	-1.50
Pdlim2	17308242	0.00181	-1.50
Ptp4a3	17312127	0.00411	-1.51
Dmd	17536078	0.00434	-1.51
LOC381967	17493653	0.00484	-1.51
Ano3	17389161	0.00842	-1.51
Slc7a3	17543529	0.00930	-1.52
Shmt1	17263673	0.00241	-1.52
Pycard	17496839	0.00767	-1.53
Ptplad2	17427051	0.00750	-1.53
Tmpo	17244191	0.00334	-1.53
Slc35f1	17233306	0.00901	-1.53
Alcam	17330918	0.00058	-1.53
Wbscr17	17453222	0.00403	-1.54
Tead4	17471278	0.00184	-1.54
Cyb5r2	17494739	0.00653	-1.54
Plxdc2	17367216	0.00338	-1.54
Inpp1	17222940	0.00051	-1.54
Abhd17c	17492978	0.00040	-1.54
Cdh2	17549842	0.00130	-1.54
Lrrtm1	17459735	0.00830	-1.54
Palm2	17414351	0.00139	-1.54
Samd5	17239142	0.00099	-1.55
Rprm	17385365	0.00704	-1.55
Ppnr	17360532	0.00521	-1.55
Dock11	17533994	0.00119	-1.55
Prss23	17493212	0.00510	-1.55
4632434I11Rik	17493358	0.00256	-1.55
C3ar1	17470616	0.00422	-1.55
Dgkh	17308842	0.00392	-1.55
Dner	17224977	0.00677	-1.55
Mylk	17325159	0.00121	-1.55
Gm13889	17388548	0.00668	-1.56

Limch1	17437887	0.00043	-1.56
Ifih1	17385797	0.00202	-1.56
Trav9d-3	17300054	0.00146	-1.56
Gpsm2	17409386	0.00621	-1.56
Tnr	17218568	0.00199	-1.57
Gm10561	17212900	0.00320	-1.57
ENSMUST0000C	17451884	0.00520	-1.57
Acy1	17530669	0.00146	-1.58
Dennd4a	17518378	0.00044	-1.58
Smarca1	17541343	0.00552	-1.58
Adra1d	17391899	0.00341	-1.58
Arhgap21	17382104	0.00049	-1.58
Eml1	17278561	0.00203	-1.59
Mlkl	17513076	0.00686	-1.59
Rps12	17239755	0.00290	-1.59
17216751	17216751	0.00764	-1.59
Notch3	17343299	0.00511	-1.59
Gm4070	17494643	0.00480	-1.59
Adam23	17213608	0.00042	-1.59
Bche	17405908	0.00339	-1.59
Zfp953	17293945	0.00282	-1.60
Gm18853	17494662	0.00937	-1.60
Bbs12	17397120	0.00183	-1.60
Pcp4	17327539	0.00545	-1.60
ENSMUST0000C	17513854	0.00471	-1.60
Tnfrsf26	17498301	0.00399	-1.60
Fras1	17439388	0.00367	-1.61
Myh10	17251370	0.00430	-1.61
Grip1	17237608	0.00031	-1.61
Mid2	17538171	0.00959	-1.61
Slc27a6	17350856	0.00419	-1.61
Morc4	17544878	0.00299	-1.61
Ptprb	17237451	0.00511	-1.62
ENSMUST0000C	17237033	0.00354	-1.62
Cdh2	17352884	0.00289	-1.62
Cnksr3	17239023	0.00195	-1.62
Vps13a	17363239	0.00104	-1.62
17415231	17415231	0.00376	-1.63
Gm20276	17547535	0.00701	-1.63
Spp1	17439830	0.00969	-1.64
Trp53cor1	17342996	0.00511	-1.64
LOC101055758	17225080	0.00051	-1.65
1190005I06Rik	17513534	0.00134	-1.65
Tceal5	17544725	0.00117	-1.65
Cspg4	17517592	0.00765	-1.66
Rspo2	17316793	0.00315	-1.66
Nkain4	17395707	0.00852	-1.66
Swap70	17481755	0.00023	-1.66
Mir1198	17533002	0.00461	-1.66
Col4a5	17538222	0.00226	-1.67

Cd109	17519738	0.00026	-1.69
Gm10855	17381511	0.00125	-1.69
Frmd3	17414913	0.00318	-1.69
Wisp1	17312022	0.00154	-1.69
Mef2c	17294682	0.00685	-1.69
Nedd9	17292071	0.00014	-1.71
Gabrb1	17438022	0.00040	-1.71
Ntn4	17236604	0.00019	-1.72
Erp27	17472199	0.00570	-1.72
Sync	17418976	0.00536	-1.72
2610016A17Rik	17363670	0.00133	-1.72
Itga11	17518191	0.00262	-1.73
Gm20038	17548135	0.00759	-1.73
Adh7	17403058	0.00337	-1.73
Arid5b	17241660	0.00202	-1.73
1700086L19Rik	17276375	0.00993	-1.74
Cyth3	17444372	0.00142	-1.74
Med13	17254629	0.00830	-1.74
Slc7a11	17405082	0.00071	-1.74
Isoc1	17350869	0.00042	-1.74
Myoc	17218752	0.00064	-1.74
Jph2	17394015	0.00797	-1.74
Maml2	17514678	0.00142	-1.74
Arhgef10	17499447	0.00050	-1.75
Itga8	17381717	0.00034	-1.75
Arhgap20	17517222	0.00656	-1.76
Robo2	17331481	0.00007	-1.76
Dock10	17224813	0.00501	-1.76
Ecscr	17353650	0.00301	-1.76
1700007K13Rik	17383373	0.00467	-1.77
Slc35f1	17240817	0.00047	-1.77
Gm9581	17331306	0.00073	-1.77
Aff3	17222465	0.00035	-1.78
Hspb1	17443342	0.00225	-1.78
8430431K14Rik	17363925	0.00637	-1.79
Slc7a11	17397421	0.00184	-1.80
Jag1	17392151	0.00094	-1.80
Myh1	17251046	0.00176	-1.80
Gm19705	17217825	0.00407	-1.81
Gpc4	17541668	0.00083	-1.82
Nexn	17411201	0.00012	-1.82
Ptk2b	17307860	0.00043	-1.83
Fmod	17217373	0.00175	-1.83
Gucy1b3	17406205	0.00155	-1.83
Ptprq	17244737	0.00020	-1.84
Pdlim1	17364474	0.00112	-1.84
Gca	17371201	0.00120	-1.84
Mtap7d3	17541856	0.00191	-1.84
Enpp5	17337844	0.00043	-1.85
Cilp	17518512	0.00457	-1.85

Fam198b	17398406	0.00012	-1.85
Prrg4	17388999	0.00005	-1.86
ENSMUST0000C	17525892	0.00379	-1.87
Gm9817	17286958	0.00015	-1.87
Arxes2	17537861	0.00299	-1.87
LOC101055663	17366278	0.00111	-1.87
Vcl	17297551	0.00164	-1.87
Gpr176	17389709	0.00012	-1.87
Spta1	17219698	0.00132	-1.88
Adamts12	17310368	0.00007	-1.88
4933400A11Rik	17546205	0.00814	-1.88
Pgm5	17363626	0.00030	-1.89
Defa-rs1	17507910	0.00638	-1.89
Slc1a6	17234833	0.00028	-1.90
Tns3	17260487	0.00035	-1.90
Mustn1	17298262	0.00332	-1.91
Col12a1	17529099	0.00036	-1.91
Olfr1318	17374214	0.00221	-1.92
Gpr64	17539271	0.00149	-1.93
Enpp4	17345124	0.00120	-1.93
Ccdc141	17387131	0.00183	-1.93
Ifit2	17358815	0.00004	-1.94
GENSCAN0000C	17548979	0.00031	-1.94
Ak5	17411235	0.00018	-1.95
Pltp	17394297	0.00046	-1.95
Gm4951	17350916	0.00559	-1.95
Tnc	17426365	0.00911	-1.96
Fmod	17227083	0.00055	-1.96
Nes	17398903	0.00029	-1.97
Gnai1	17445735	0.00171	-1.97
Myh2	17251001	0.00136	-1.97
Gas2	17478476	0.00181	-1.97
Slfn2	17254166	0.00368	-1.97
Lmo7	17302429	0.00013	-1.99
Galnt18	17495172	0.00145	-1.99
Calml4	17518238	0.00137	-1.99
Itga4	17372307	0.00562	-2.01
Gm19274	17548671	0.00168	-2.02
Cryab	17548750	0.00013	-2.03
Cd80	17325608	0.00010	-2.03
Foxs1	17393004	0.00151	-2.04
Lmcd1	17461477	0.00014	-2.04
Upk1b	17330427	0.00520	-2.05
Edn1	17286830	0.00003	-2.06
Col8a1	17331162	0.00148	-2.07
Gm13362	17382101	0.00019	-2.07
Lims2	17349209	0.00114	-2.10
Susd2	17241849	0.00039	-2.10
Pld5	17230176	0.00210	-2.11
Mtss1	17317327	0.00012	-2.11

Adamts1	17331705	0.00023	-2.12
Etl4	17367390	0.00026	-2.14
Bmp3	17439535	0.00007	-2.14
Meox2	17275062	0.00026	-2.14
Pi15	17211305	0.00021	-2.15
Fhl2	17222642	0.00022	-2.15
Fam101b	17266038	0.00068	-2.15
Serpine1	17453819	0.00144	-2.18
Ccdc80	17325904	0.00059	-2.19
Tslp	17349304	0.00031	-2.19
2310022B05Rik	17514087	0.00005	-2.20
Cntnap3	17293721	0.00425	-2.20
Adamts14	17547499	0.00575	-2.21
Fat3	17524233	0.00020	-2.21
ENSMUST0000C	17297591	0.00003	-2.22
GM8989	17494664	0.00362	-2.24
Pdlim3	17500922	0.00215	-2.25
Sdpr	17212719	0.00177	-2.25
Cryab	17517132	0.00019	-2.29
4833412C05Rik	17492031	0.00161	-2.30
Adh1	17403070	0.00252	-2.30
Cdc42ep3	17347435	0.00021	-2.30
Abi3bp	17326318	0.00235	-2.33
Ppp1r14a	17476119	0.00109	-2.38
Figf	17539536	0.00809	-2.38
Tnfsf18	17218707	0.00245	-2.38
Rcan2	17337834	0.00026	-2.39
Sorbs2	17500876	2.9E-06	-2.40
Gpr126	17239435	0.00033	-2.42
Eln	17453454	0.00062	-2.42
F11r	17219362	0.00165	-2.44
Ccdc80	17330612	0.00265	-2.50
Insc	17482047	0.00007	-2.51
Mir3093	17399008	0.00069	-2.54
Arhgef6	17541875	0.00009	-2.55
Col14a1	17311551	0.00003	-2.56
ENSMUST0000C	17550036	0.00420	-2.58
Pawr	17237170	0.00102	-2.60
Lbh	17339554	0.00240	-2.65
Phxr4	17514687	0.00040	-2.66
Klf5	17302397	0.00001	-2.68
Flt1	17455346	0.00022	-2.69
Ptprz1	17456381	0.00021	-2.69
Cpa6	17221269	0.00018	-2.71
Adrb2	17354857	0.00002	-2.74
n412642	17381351	0.00172	-2.78
Gm4070	17494651	0.00122	-2.91
Adm	17481770	0.00006	-2.91
Itgbl1	17302936	0.00002	-2.98
Sprr3	17407407	0.00040	-3.05

Ctgf	17232235	0.00451	-3.15
Gm10808	17547949	0.00312	-3.30
Bex1	17544734	0.00505	-3.55
9930013L23Rik	17492947	0.00826	-3.66
Trav9d-3	17300247	0.00033	-3.68
Map3k7cl	17326887	0.00017	-4.02
Gucy1a3	17406221	0.00008	-4.62
Ccl20	17214857	0.00012	-4.63
Meox1	17269974	4.8E-06	-5.23
Prl3a1	17286158	1.1E-06	-9.05

Supplemental Figures and Legends

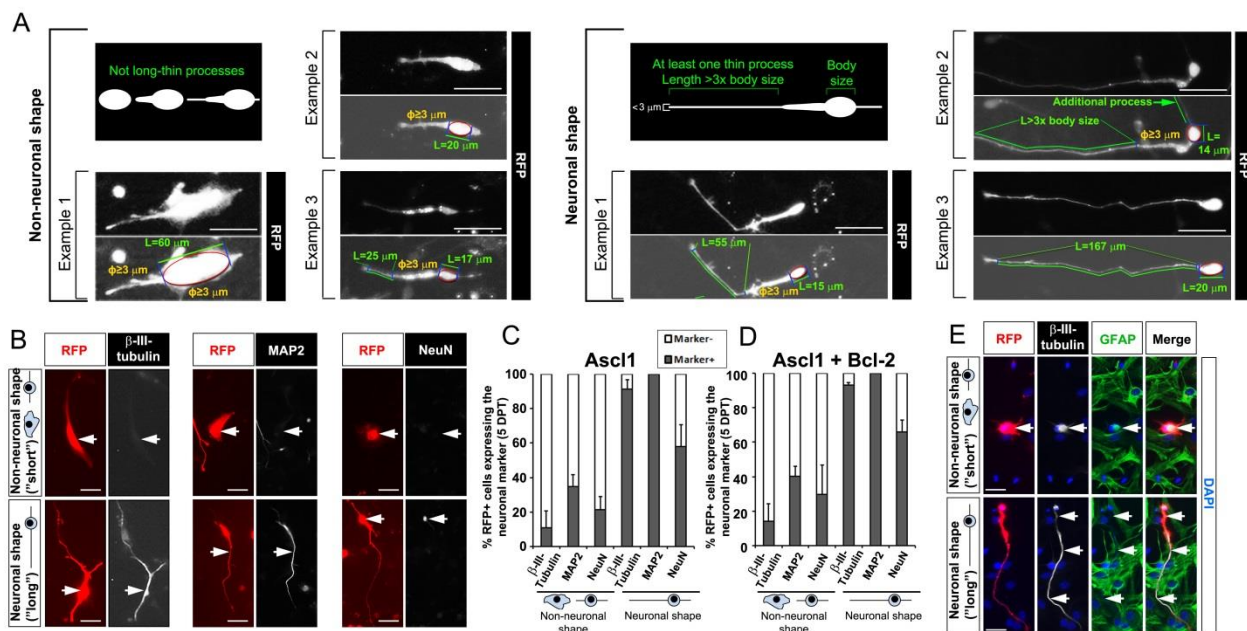


Figure S1. Related to Figure 1

Validation of the Morphological Criteria.

(A) Description of the morphological criteria used to classify cells as “non-neuronal/astroglial” or “neuronal” in the time-lapse movies. Cells with at least one thin process ($\phi < 3\ \mu\text{m}$) $3\times$ longer than the soma were classified as “neuronal”. The cell soma was designated as an ellipsoid located at the most prominent swelling part of the cell, at the level where the nucleus is located (visible by accumulation of RFP fluorescence). The largest diameter of the ellipsoid was measured and compared to the length of the longest thin process (see examples). For the morphometric analysis and the video tracking of single cells we used the software ImageJ (FIJI version).

(B) Examples of astrocytes transfected with *Asc11* and RFP-encoding plasmid at 5 DPT classified according to morphological criteria. Cells classified as neurons (lower panels) are immune-reactive for the neuronal markers β -III-tubulin, MAP2 and NeuN, contrary to cells with an astrocyte morphology (upper panels).

(C, D) Histograms show quantifications of the analysis from B in cultures transfected with *Asc11*/RFP alone (C) or in combination with *Bcl-2* (D).

(E) Immunocytochemistry showing that some “non-neuronal/astroglial” cells (upper panels) transduced with *Asc11* co-express both neuronal (β -III-tubulin, white) and astroglial (GFAP, green) markers at 5 DPT. Contrarily, cells with neuronal morphology (lower panels) only express neuronal markers (β -III-tubulin).

Error bars indicate \pm SD. Scale bars: $20\ \mu\text{m}$ in (B, E) and $40\ \mu\text{m}$ in (A).

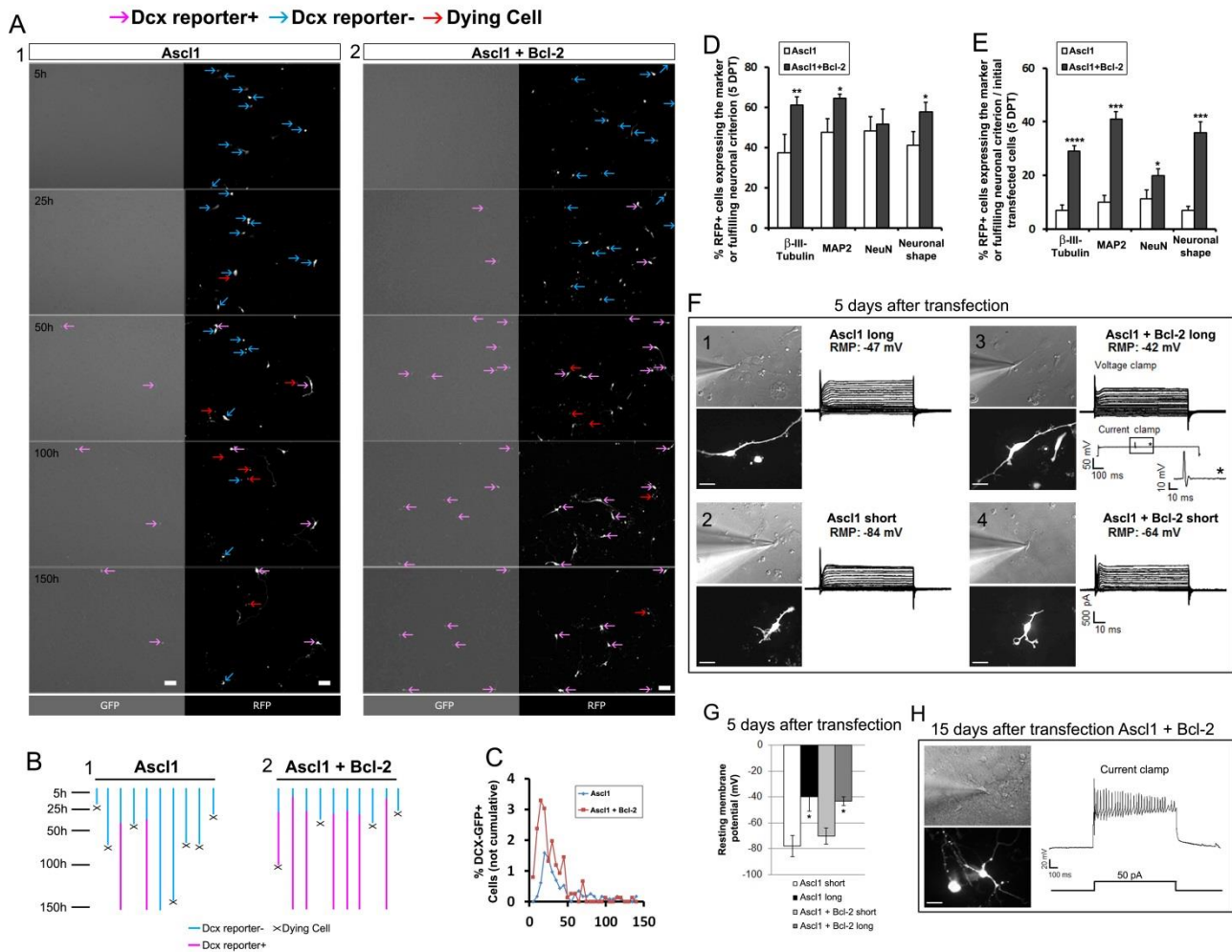


Figure S2. Related to Figure 2

Analysis of Neuronal Conversion by DCX-GFP, Expression of Neuronal Markers and Electrophysiology.

(A) Still images from time-lapse movies (Figure 1A and Movie S2) show astroglial cells (blue arrows), DCX-GFP+ neurons (purple arrows, GFP reporter column) and dying cells (red arrows) at different time points in cultures co-transfected with only DCX-GFP and *Ascl1* (left panels) or in combination with *Bcl-2* (right panels).

(B) Progeny-trees of single cells tracked from the examples in A showing that cells rarely proliferate during reprogramming. Most astroglial cells (blue lines) do not turn directly into DCX-GFP neurons (purple lines) and die (depicted with “x”) before converting.

(C) Percent of transfected cells that newly acquire DCX-GFP signal at different time-points in the movies from A. 1095 and 220 cells were counted in *Ascl1* and *Ascl1+Bcl-2*, respectively.

(D, E) Histograms showing the percent of cells immune-reactive for neuronal markers or having a neuronal shape, as indicated, among the transfected (RFP+) cells at 5 DPT (N=3).

(F) Patch-clamp recordings from the cells transfected with only *Ascl1/RFP* (1-2) or in combination with *Bcl-2* (3, 4) at 5 DPT. The left panels show brightfield with a patch electrode attached (up) and red-fluorescence (down). On the right, the resting membrane potential and voltage-clamp is shown for all the examples. In the example 3, a current-clamp displays very immature action potential-like features elicited by co-transfection with *Ascl1/RFP* and *Bcl-2*.

(G) Histogram shows quantification of resting membrane potential (RMP) in short/long cells transfected with only *Ascl1* or in combination with *Bcl-2*. N=6 cells in *Ascl1/long-short* cells; N=10 cells in *Ascl1+Bcl-2/long* cells; N=8

cells in *Ascl1*+*Bcl-2*/short cells. Note that a higher number of cells has a neuronal morphology upon *Bcl-2* co-transduction (E) and hence a higher number of cells has a more positive RMP.

(H) Recordings from a cell transfected with *Ascl1* and *Bcl-2* at 15 DPT show a current-clamp trace elicited by 50 pA current injection with notable mature action potentials.

Error bars indicate \pm SD. *p 0.05, **p<0.01, ***p<0.001, ****p<0.0001; unpaired t test in D, E, G. Scale bars 50 μ m in A, 40 μ m in F, H.

See also Movie S2.

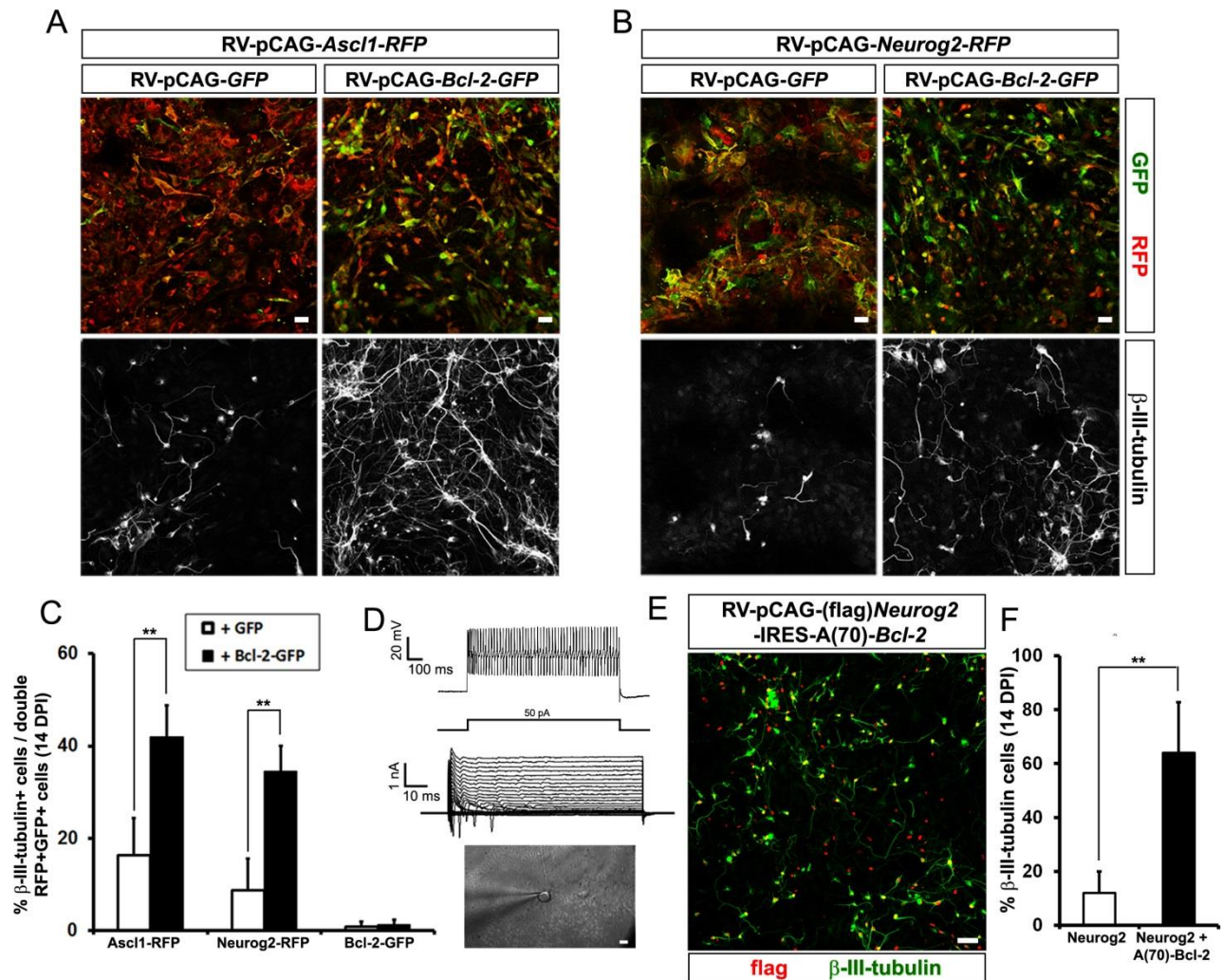


Figure S3. Related to Figure 3

Bcl-2 and A(70)-Bcl-2 Enhance Neuronal Conversion of MEFs.

(A, B) Epifluorescence images of MEF cultures co-infected with *Ascl1*/RFP- (A) or *Neurog2*/RFP- (B) encoding viral vectors in combination with the *GFP* control or *Bcl-2*/GFP-encoding viral vectors. Note that *Bcl-2* increases the number of neurons immunoreactive for β -III-tubulin obtained at 14 DPI (lower panels; white cells).

(C) Histogram showing the quantifications of experiments from A and B (N=4).

(D) Electrophysiological recordings from the cell infected with *Ascl1* and *Bcl-2* and shown in brightfield in the lowest panel with a patch electrode attached. On the top panel, a current-clamp trace elicited by 50 pA current injection is shown revealing a train of action potentials, while the middle panel shows voltage-clamp traces with notable fast-inactivating inward currents.

(E) Epifluorescence images of MEF cultures transduced with the retroviral vector *Neurog2*-IRES-A(70)-*Bcl-2*. Note the high proportion of neurons immunoreactive for β -III-tubulin (green) among the transduced population (flag+; red).

(F) Histogram showing the high increase in the conversion efficiency mediated by *Neurog2*- and A(70)-*Bcl-2*-co-expression compared to the *Neurog2*-only transduced controls (N=3).

Error bars indicate \pm SD. ** $p < 0.01$; unpaired t test in C, F. Scale bars: 40 μ m.

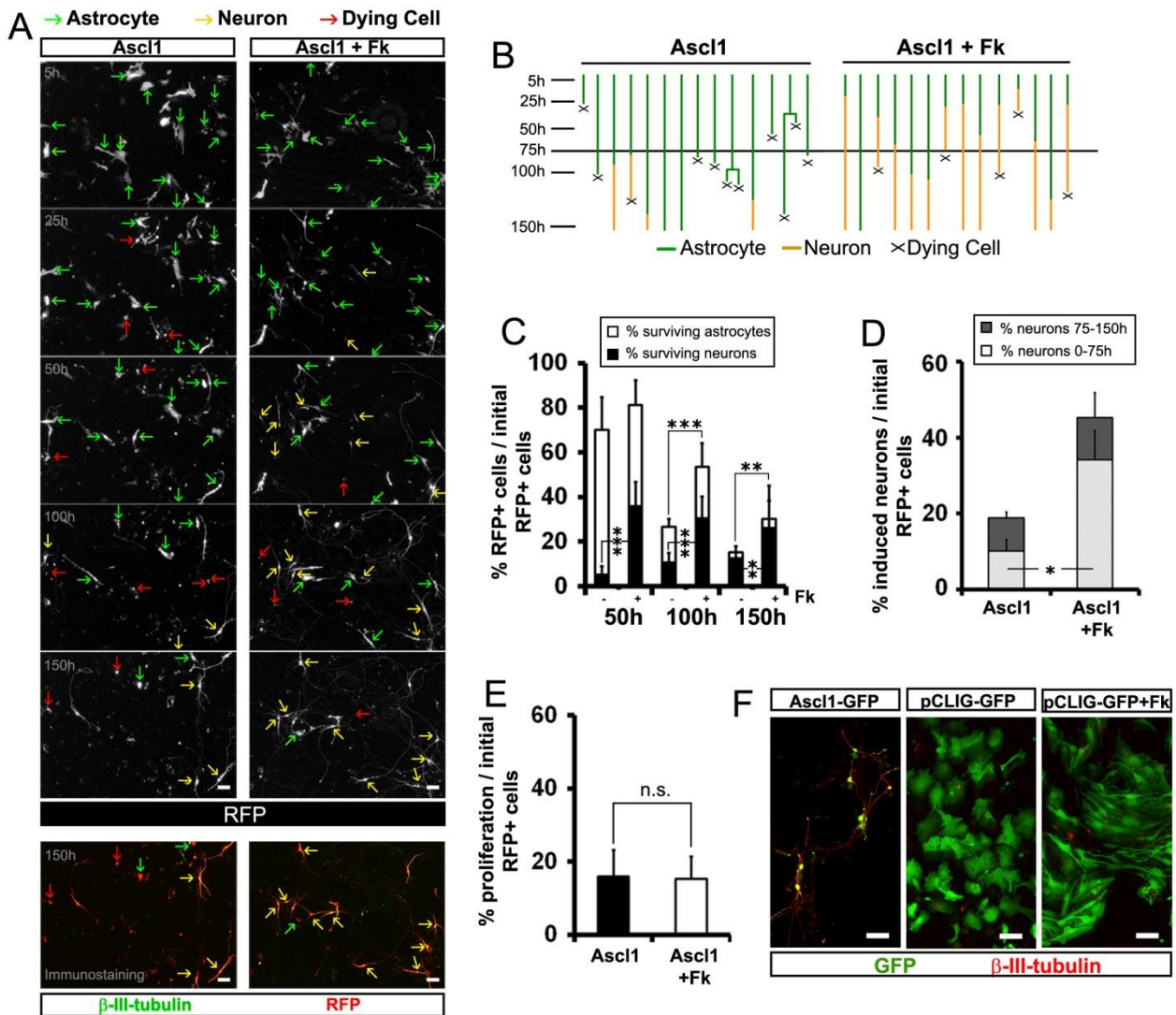


Figure S4. Related to Figure 4

Analysis of Astrocyte-to-Neuron Conversion upon Forskolin Treatment by Live Imaging.

(A) Examples of still images from time-lapse movies (see Movie S3) show astroglial cells (green arrows), neurons (yellow arrows) and dying cells (red arrows) at different time points, in the presence or absence of Fk. Last image shows immunostaining of fixed cells confirming that all RFP+ cells are neurons (yellow arrows) expressing β -III-tubulin (green). Note that at the end of the movie, the number of neurons increased in Fk treated cultures (20 μ M).

(B) Progeny-trees of single cells tracked from example in A showing that cells rarely proliferate during reprogramming and most astroglial cells (green lines) die (dead cells depicted with "x") before they could become neurons (yellow lines). Fk treatment (right diagram) resulted in faster acquisition of neuronal morphology, reduced cell death and increased reprogramming efficiency.

(C) Analysis of neuronal conversion and cell survival during the observation period, in Fk treated and untreated cultures. The total number of astrocytes/neurons (white and black bars, respectively) is normalized to the initial number of transfected cells analysed at 1 DPT.

(D) Histogram showing that neurons appear mostly in the first half of imaging time upon Fk treatment.

(E) Histogram of the proportion of *Ascl1*-transfected cells proliferating during 150 h of observation with or without Fk treatment. Note that this value is low and not significantly increased upon Fk treatment.

(F) Micrograph showing that Fk does not induce neuronal conversion of astrocytes (β -III-tubulin, Red) without the expression of neuronal fate determinants.

N=5 in the control condition (339 initial tracked cells); N=4 in Fk treated condition (195 cells).

Error bars indicate \pm SD. * $p < 0.05$, ** $p < 0.01$, *** $p < 0.001$, $p \geq 0.05$ no statistically significant difference (n.s.); ANOVA with Tukey's post-hoc test in C; unpaired t test in D, E. Scale bars: 40 μ m.

See also Movie S3.

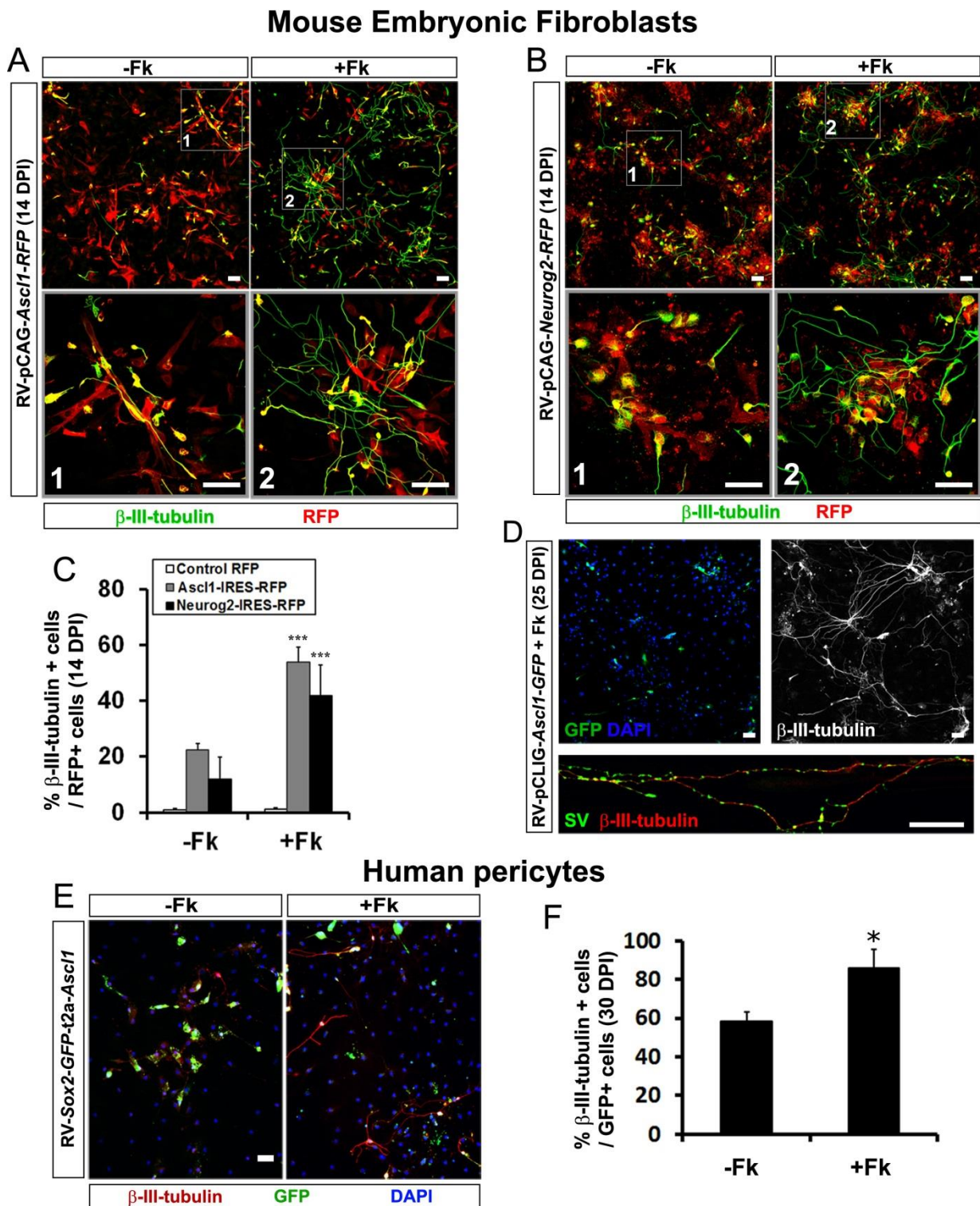


Figure S5. Related to Figure 5

Widespread Effect of Forskolin in Enhancing Neuronal Reprogramming

(A, B) Micrographs showing *Ascl1*- or *Neurog2*-transduced MEFs analysed for β -III-tubulin immunoreactivity (green) 14 days after retroviral infection. MEF-derived neurons exhibit longer and more complex processes upon Fk treatment (boxed areas 1 and 2 magnified in the lower panels).

(C) Histogram showing the proportion of β -III-tubulin+ neurons amongst control (white bars), *Ascl1* (grey bars) or *Neurog2* (black bars) transduced (RFP+) MEFs upon Fk treatment (N=3).

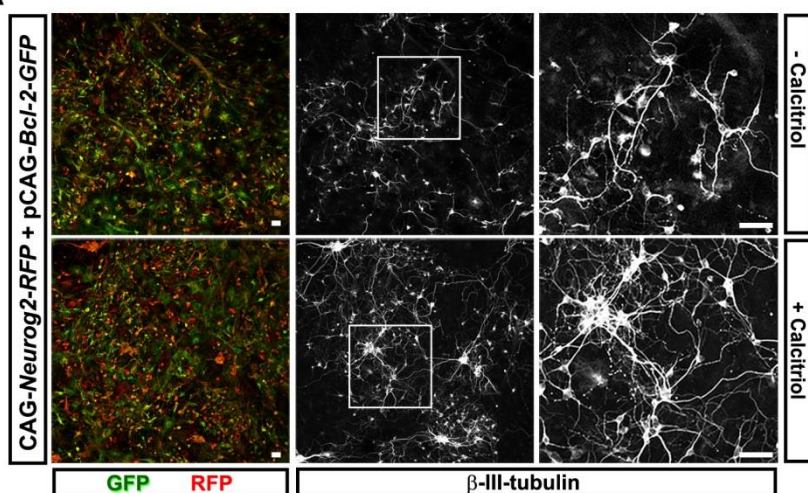
(D) Micrograph showing highly complex β -III-tubulin+ processes (upper right panel) of *Ascl1*-infected MEFs (upper left panel, green cells) upon Fk addition at 25 DPI. Lower panel shows high magnification view of β -III-tubulin+ (red) neurites with high density of synaptobrevin (SV) puncta (green) indicating synaptic contacts.

(E) Epifluorescence images of human pericyte-derived neurons showing β -III-tubulin-immunoreactivity (red) 4 weeks after infection with a viral vector co-expressing *Ascl1*, *Sox2* and *GFP* (green) in cultures with (right panels) or without Fk addition. After Fk treatment neurons show more mature morphology, with more complex and extended neurites.

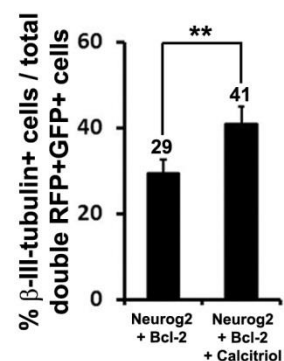
(F) Histogram depicting the proportion of β -III-tubulin-immunoreactive cells from (E) amongst all GFP+ transduced cells (N=3).

Error bars indicate \pm SD. Statistical tests performed on treated and untreated cells transduced with the same transcription factor (Control, *Ascl1*, *Neurog2*, *Dlx2*). * $p < 0.05$, ** $p < 0.01$, *** $p < 0.001$; unpaired t test. Scale bars: 40 μ m.

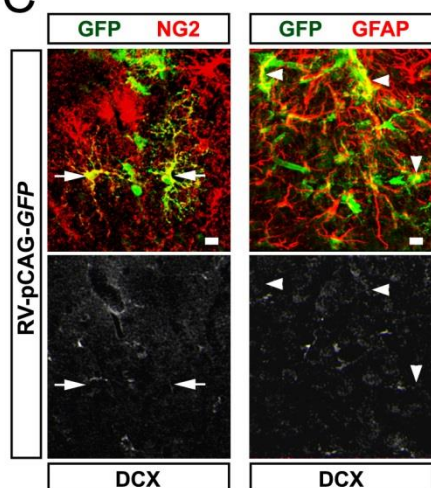
A



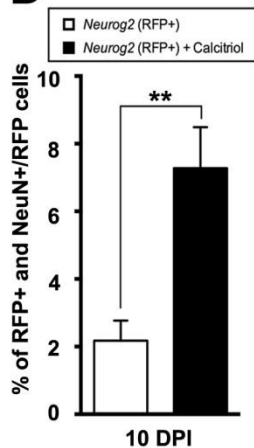
B



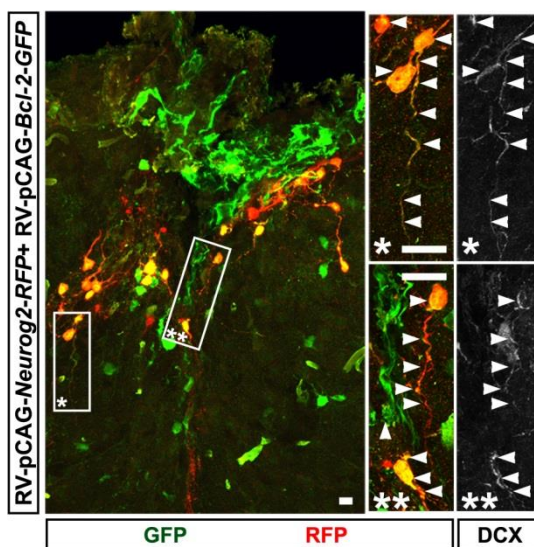
C



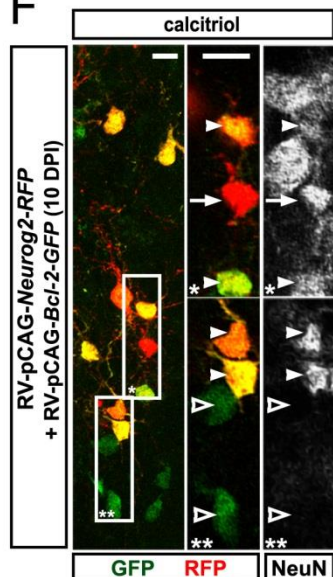
D



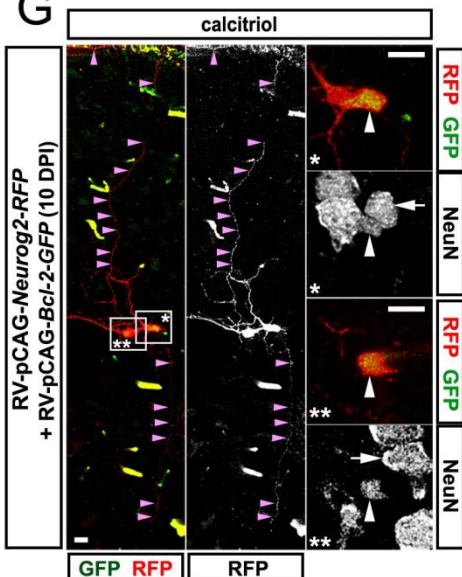
E



F



G



H

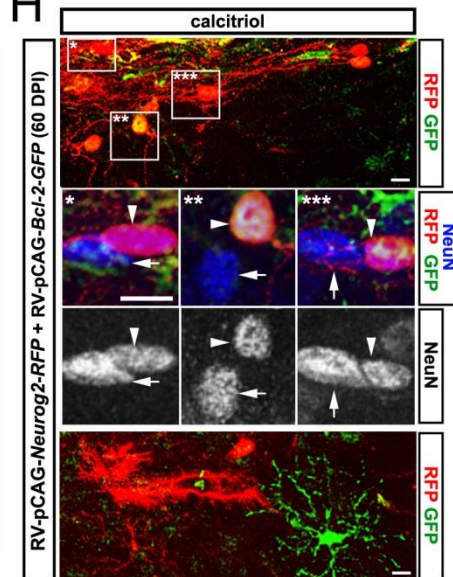


Figure S6. Related to Figure 6

Calcitriol Enhances Neurog2-Mediated Reprogramming of MEFs *In Vitro* and Glial Cells After stab wound Injury *In Vivo*.

(A) Epifluorescence micrographs of MEF cultures 10 days after co-transduction with *Neurog2/RFP* and *Bcl-2/GFP* in the absence (upper row) or presence (lower row) of calcitriol. Higher magnification (right column) of the insets shows the beneficial effects of calcitriol.

(B) Histogram depicting the proportion of β -III-tubulin-immunoreactive cells amongst the MEFs co-infected with *Neurog2/RFP* and *Bcl-2/GFP* with or without calcitriol, at 10 days after retroviral transduction.

(C) Confocal micrographs (maximum intensity projection) of cells infected by the retroviral vector encoding for *GFP in vivo* after stab-wound injury and immunostained for NG2, GFAP and Doublecortin (DCX) at 7 days post-injection (DPI). GFP+ cells are NG2+ (left panel, arrow) or GFAP+ (right panels, arrowheads). No DCX+ cells were detected around the lesion site.

(D) Quantifications of NeuN/RFP double-positive cells after stab-wound injury and subsequent injection with *Neurog2/RFP in vivo*. Mice were treated or not with calcitriol and analysed at 10 DPI as depicted in Figure 6A.

(E) Confocal micrographs of the injection site (10 DPI, maximum intensity projection) and immunohistochemistry for DCX. The cells in the insets (*,**) are shown at higher magnification, with white arrowheads indicating the co-localization of the processes with DCX.

(F) Cells infected by *Neurog2/RFP* alone or with *Bcl-2/GFP* after stab-wound injury *in vivo*, analyzed at 10 DPI after treatment with calcitriol (Figure 6A), with magnified single optical sections (*,**) shown on the right. Some RFP+ cells (transduced with *Neurog2* only) are NeuN-immunopositive (arrow), whereas GFP+ cells (transduced only with *Bcl-2*) never do (empty arrowheads). Co-infected cells are frequently NeuN+ (filled arrowheads).

(G) Confocal micrographs (maximum intensity projection) showing neurons co-transduced *in vivo* (10 DPI) after treatment with calcitriol. Purple arrowheads indicate neurites emerging from adjacent neurons and growing towards the pial surface (above) and the white matter (below). High magnification panels on the right (*,**) show that both neurons have high levels of NeuN (white arrowheads), comparable to those found in native neurons around the same area (white arrows).

(H) Confocal micrographs (maximum intensity projection) of cells co-infected by *Neurog2/RFP* and *Bcl-2/GFP* (magnified in boxes *, ** and ***; arrowheads) after treatment with calcitriol are immunoreactive for NeuN at 60 DPI. Note that their soma size is comparable to the one displayed by surrounding endogenous neurons (arrows). The picture at the bottom shows single infected cells (RFP+ or GFP+) still viable after 60 DPI and maintaining their glial nature. Error bars indicate \pm SD. N=1 in C, E, H; N=3 in A, B, D, F, G **p<0.01; unpaired t test in B, D. Scale bars: 40 μ m in A and 10 μ m in C, E, F-H.

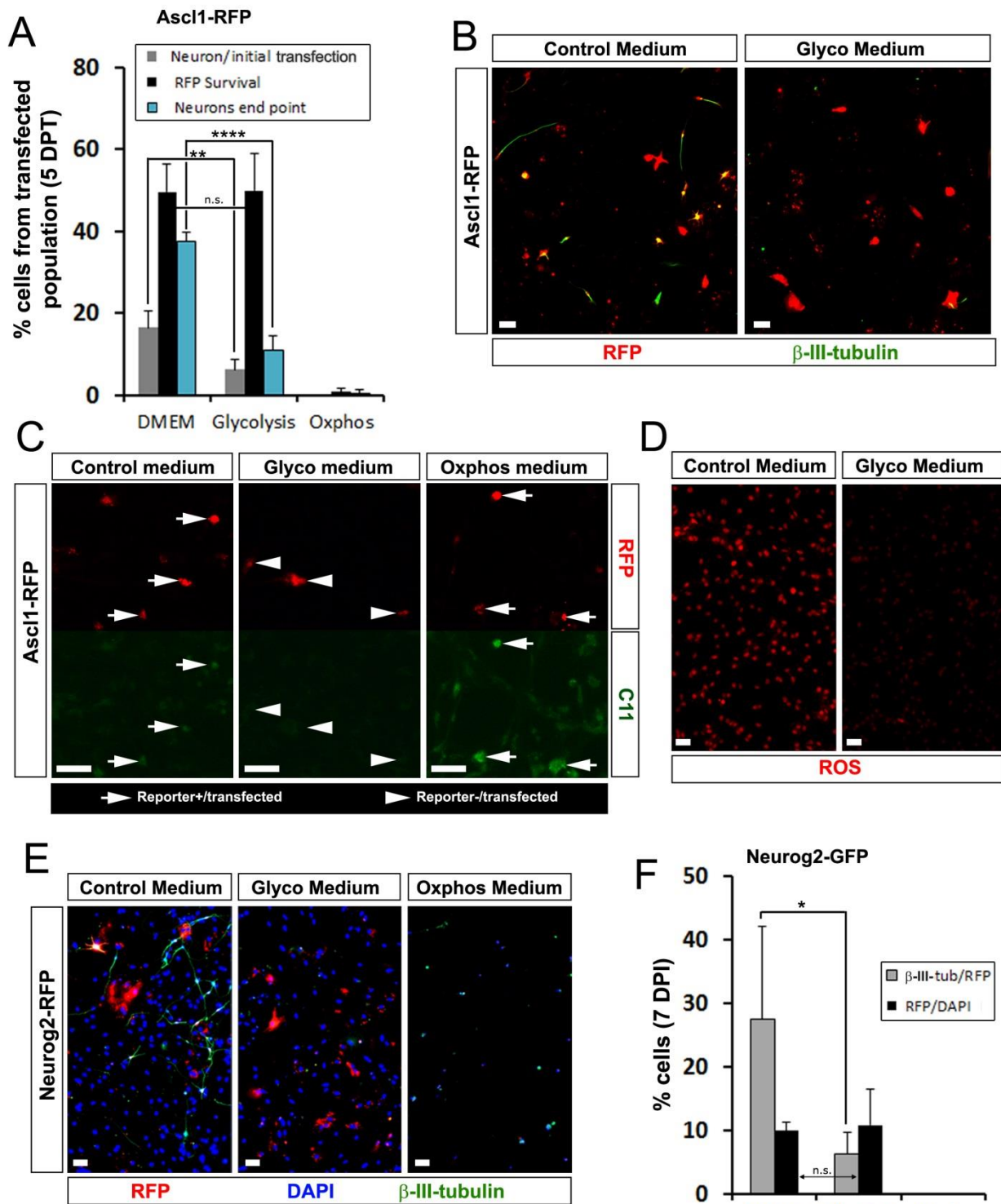


Figure S7. Related to Figure 7

Maintaining Glycolysis in Astroglial Cells Reduces Oxidative Stress but Blocks Reprogramming Into Neurons.

(A) Quantification of experiments with examples of cells shown in B depicting the % of neuronal conversion normalized to the initial number of transfected cells (1 DPT; grey bars), at the end point (5 DPT; blue bars) and % of surviving cells (black bars) grown in anaerobic glycolysis-only, OxPhos-only or control medium. Note that all cells grown in OxPhos medium die, while cells grown in anaerobic glycolysis medium survive but fail to convert into neurons.

(B) Micrographs of astroglial cultures transfected with *Ascl1/RFP* and maintained in culture for 5 days in normal differentiation medium (control medium) or anaerobic glycolysis medium. As previously, neuronal conversion was monitored by β -III-tubulin immunoreactivity (green) among the transfected population (RFP+, red). Note that cells in glycolysis only medium do not acquire β -III-tubulin.

(C) Micrographs showing representative examples of Lip-Ox evaluated by C11-Bodipy reaction (green channel), of *Ascl1/RFP* transfected cells (RFP+, red) 24 hours after change with medium capable of inducing selective metabolisms (control medium, anaerobic glycolysis-only medium, OxPhos-only medium). Arrows indicate transfected cells (red) with increased levels of Lip-Ox (green); arrowheads transfected cells without green signal. Note that anaerobic glycolysis medium reduces Lip-Ox in transfected cells, while OxPhos medium potentially increases it compared to Control medium.

(D) Micrographs of astroglial culture at 24h in the anaerobic glycolysis-only medium already shows much reduced ROS signal detected by the superoxide indicator dye Dihydroethidium (DHE, 5 μ M, Life Technologies), which shifts from a blue fluorescence in the cytosol to a red fluorescence in the nucleus when oxidized.

(E) Micrographs of astroglial cultures transduced with *Neurog2/RFP* and maintained 7 days in normal differentiation medium (control Medium, left), anaerobic glycolysis-only medium (middle) or OxPhos-only medium (right). Neuronal conversion was monitored by β -III-tubulin immunoreactivity (green) among the transfected cells (RFP+, red). Note that also *Neurog2*-induced reprogramming is impaired in anaerobic glycolysis medium, while cells do not survive in OxPhos-only metabolism.

(F) Quantification of the experiment in E showing that the % of neuronal conversion normalized to the final number of transduced cells (β -III-tubulin/RFP at 7 DPI; grey bars) is drastically reduced when cells are grown in anaerobic glycolysis medium, while % of surviving cells (RFP/total DAPI at 7 DPI; black bars) is unaffected.

Error bars indicate \pm SD. * $p < 0.05$, ** $p < 0.01$; **** $p < 0.0001$; ANOVA with Tukey's post-hoc test in A; ANOVA with Holm-Sidak's post-hoc test in F. Scale bars: 40 μ m.

Supplemental tables

Table S1 as Excel file. Related to Figure 5

Genes Regulated by Forskolin. Microarray analysis of MEF cultures treated or not with Fk. All cells were transduced with an Ascl1/RFP- encoding vector. Shown are 507 probe sets regulated in Ascl1+Fk vs Ascl1 as defined by $p < 0.01$, fold change $\geq 1.5x$, and average expression in at least one group in the dataset > 20 arbitrary units. See Excel file.

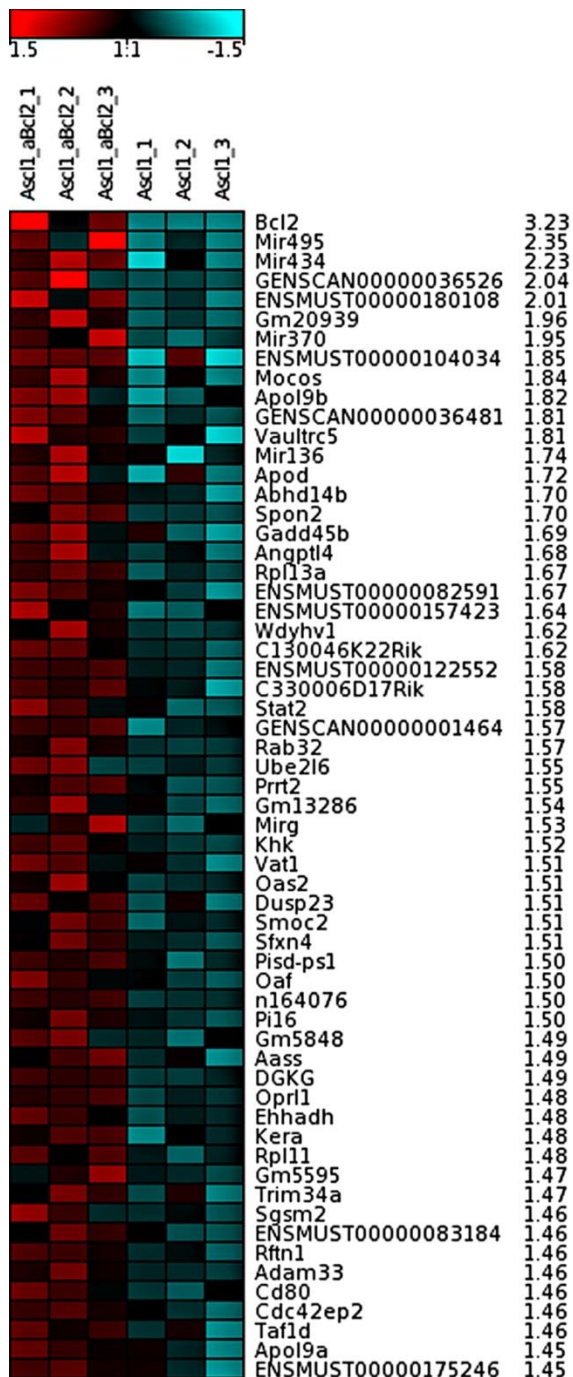


Table S2. Related to Figure 5

Genes Regulated by A(70)-Bcl-2. Table shows heatmaps of the top 60 up-regulated genes based on microarray analysis (Ascl1+A(70)-Bcl-2 vs Ascl1; $p < 0.01$, fold-change ≥ 1.45). Linear fold-changes are indicated.

Ingenuity Canonical Pathways associated with up-regulated genes	-log(p-value)	Molecules
Axonal Guidance Signaling	5.76	SLIT3, ENPEP, PAPP2, FZD3, BMP2, CXCL12, EPHA4, PLXNA2, GNA14, FZD1, ADAMTS2, SEMA4C, PRKAG1, TUBB2B, SRGAP1, WNT4, PRKD1, PRKCA, BMP1, GNG4, PAPP2, TUBB3, SEMA5A, CHP1, TUBA4A, FZD9, NFATC4, BMP5, NTRK2, ADAM12, EPHA5, BMP7
cAMP-mediated signaling	5.69	GRK4, ADCY2, PDE7A, VIPR2, PDE10A, CNR1, PDE3A, STAT3, PDE4B, PDE1A, PDE1C, PDE8A, S1PR3, ADCY9, LPAR1, PDE7B, PDE3B, ADCY5, PDE8B, AGTR2, AGTR1
PPARα/RXRα Activation	6.89	ADCY2, IL1RL1, TGFB3, BCL3, IL6, GNA14, IL1R1, NFKB2, ABCA1, PRKAG1, ACVR1B, IL1R2, NR2F1, TGFB2, ADCY9, JUN, IL1RL2, ADCY5, GPD2, PRKCA
IL-10 Signaling	6.30	IL33, IL1R2, SOCS3, IL4R, JUN, IL1RL2, IL1RL1, STAT3, IL1R1, LBP, NFKB2, IL6
PPAR Signaling	4.11	IL33, PPARG, IL1R2, NR2F1, JUN, IL1RL2, IL1RL1, PDGFRA, IL1R1, PTGS2, NFKB2
LXR/RXR Activation	3.36	IL33, IL1R2, IL1RL2, IL1RL1, LBP, PTGS2, NFKB2, IL6, PON3, ABCA1
LPS/IL-1 Mediated Inhibition of RXR Function	3.01	MGST1, CPT1A, IL1RL1, IL1R1, SOD3, ABCA1, IL33, IL1R2, JUN, IL1RL2, CHST11, ACSL4, HS3ST1, LBP, ACSL1
Wnt/β-catenin Signaling	2.85	FZD3, TGFB3, LRP6, FZD9, KREMEN1, FZD1, SOX11, ACVR1B, TGFB2, JUN, WNT4, SOX9, SFRP1
BMP signaling pathway	2.83	SOSTDC1, JUN, BMP2, BMP7, NFKB2, BMP5, PRKAG1, BMP1
IL-9 Signaling	2.47	SOCS3, IRS2, BCL3, STAT3, NFKB2
NF-κB Signaling	2.45	IL33, IL1R2, TGFB2, TNFSF11, NTRK2, TGFB3, BMP2, PDGFRA, FGFR2, IL1R1, NFKB2, IRAK3
IL-17 Signaling	2.42	JUN, TIMP1, CEBPB, PTGS2, IL6, IL17RA, CCL11
STAT3 Pathway	2.18	TGFB2, SOCS3, NTRK2, TGFB3, PDGFRA, FGFR2, STAT3
VDR/RXR Activation	2.03	TNFSF11, IL1RL1, CEBPB, VDR, S100G, PRKD1, PRKCA
HGF Signaling	1.91	JUN, ETS2, HGF, STAT3, PTGS2, IL6, PRKD1, PRKCA
NRF2-mediated Oxidative Stress Response	1.86	MGST1, SOD2, JUN, MAF, JUND, GCLM, NFE2L2, TXNRD1, SOD3, PRKD1, PRKCA
FGF Signaling	1.83	FGF21, FGF10, HGF, FGFR2, STAT3, FGF7, PRKCA
TGF-β Signaling	1.83	TGFB2, JUN, BMP2, BMP7, VDR, INHBB, ACVR1B
CXCR4 Signaling	1.83	GNG4, ADCY9, ADCY2, JUN, ADCY5, CXCL12, RHOU, GNA14, PRKD1, PRKCA
JAK/Stat Signaling	1.66	SOCS3, JUN, STAT3, CEBPB, NFKB2, IL6
Ingenuity Canonical Pathways associated with down-regulated genes	-log(p-value)	Molecules
Axonal Guidance Signaling	1.32	BMP4, ADAMTS1, PDGFA, BMP3, GNA11, VEGFC, ABLIM1, FZD8, SEMA3A, RRAS2, PRKAR2B, SEMA3D, PAK3, ARHGEF6, ADAM23, FIGF, ROBO2, ADAMTS5, ITGA4
VEGF Signaling	2.32	RRAS2, PTK2B, ACTA2, FLT1, VEGFC, FIGF, VCL, BCL2
Death Receptor Signaling	1.32	GAS2, ACTA2, HSPB2, PARP14, HSPB1, BCL2

Table S3. Related to Figure 5

Analysis of Pathways Regulated by Forskolin. Enrichment analysis of canonical pathways based on the set of 1321 probe sets differentially regulated between MEF cultures treated or not with Fk (fold change>1.3x, p<0.05, Av>20). All cells were transduced with an Ascl1/RFP- encoding vector. Analysis was done separately for up- and down-regulated probes using Ingenuity Pathway Analysis software and selected significantly enriched terms (p<0.05) are shown.

Ingenuity Canonical Pathways associated with up-regulated genes	-log(p-value)	Molecules
NRF2-mediated Oxidative Stress Response	5.74	MGST1, MAF, HSPB8, DNAJC15, JUNB, CLPP, GSTO1, GSR, DNAJC4, CAT, DNAJA3, JUND, GCLM, NFE2L2, GSTP1, MGST3, GSTK1
Granulocyte Adhesion and Diapedesis	5.09	HRH2, VCAM1, IL1RL1, PF4, IL1R1, CCL5, CCL11, CXCL6, IL33, IL1RL2, CCL7, Ccl2, PPBP, CXCL2, MMP19
Glutathione-mediated Detoxification	4.85	MGST1, ANPEP, GSTP1, GSTO1, MGST3, GSTK1
Role of Macrophages, Fibroblasts and Endothelial Cells in Rheumatoid Arthritis	4.36	SOCS3, VCAM1, FRZB, IL1RL1, CHP1, WNT2B, IRAK3, STAT3, IL1R1, CCL5, IL17RA, PRSS3, TLR2, IL33, FZD4, IL1RL2, LTBR, SFRP1, WNT5A, CAMK2G
LXR/RXR Activation	3.97	IL33, FDFT1, IL1RL2, CCL7, IL1RL1, LPL, SERPINA1, IL1R1, PTGS2, NFKB2, RXRA
IL-10 Signaling	3.62	IL33, SOCS3, IL4R, IL1RL2, IL1RL1, STAT3, IL1R1, NFKB2
Agranulocyte Adhesion and Diapedesis	3.55	IL33, VCAM1, CCL7, Ccl2, PF4, PPBP, CCL5, IL1R1, CXCL2, CCL11, CD34, CXCL6, MMP19
Glutathione Redox Reactions I	3.34	GSR, MGST1, MGST3, GSTK1
Hepatic Fibrosis / Hepatic Stellate Cell Activation	3.14	IGFBP4, IL4R, VCAM1, IL1RL2, TIMP1, IL1RL1, PDGFRA, IL1R1, CCL5, NFKB2, AGTR1
IL-9 Signaling	2.80	SOCS3, IRS2, BCL3, STAT3, NFKB2
LPS/IL-1 Mediated Inhibition of RXR Function	2.74	IL33, MGST1, IL1RL2, CYP3A5, IL1RL1, CAT, IL1R1, RXRA, MGST3, GSTP1, GSTO1, SULT2A1, GSTK1
PPAR Signaling	2.71	IL33, IL1RL2, IL1RL1, PDGFRA, IL1R1, PTGS2, NFKB2, RXRA
Role of IL-17A in Arthritis	2.70	CCL7, CCL5, PTGS2, NFKB2, IL17RA, CXCL6
Xenobiotic Metabolism Signaling	2.47	MGST1, MAP3K6, MAF, NFKB2, SULT2A1, GSTO1, CYP3A5, CAT, RXRA, NFE2L2, GSTP1, MGST3, CAMK2G, GSTK1
Geranylgeranyldiphosphate Biosynthesis	2.42	COX10, GGPS1
Hepatic Cholestasis	2.21	IL33, IL1RL2, IL1RL1, IL1R1, NFKB2, IRAK3, RXRA, PRKAG1, ATP8B1
Mitochondrial Dysfunction	2.19	GSR, NDUFS5, COX10, CAT, NDUFA7, SDHD, CYB5A, BACE2, UQCRCQ, PSEN1
Acute Phase Response Signaling	2.09	IL33, C1R, SOCS3, SERPINA3, OSMR, SERPINA1, STAT3, IL1R1, NFKB2, RBP1
Gai Signaling	2.01	S1PR3, CNR1, GNG5, STAT3, AGTR2, AGTR1, PRKAG1, OPRL1
IL-17A Signaling in Fibroblasts	1.98	CCL7, LCN2, NFKB2, IL17RA
Role of IL-17F in Allergic Inflammatory Airway Diseases	1.77	CCL7, NFKB2, IL17RA, CXCL6
Aryl Hydrocarbon Receptor Signaling	1.74	MGST1, NFKB2, RXRA, NFE2L2, GSTP1, GSTO1, MGST3, GSTK1
cAMP-mediated signaling	1.72	PDE8A, AKAP12, S1PR3, HRH2, PDE7B, CNR1, STAT3, AGTR2, AGTR1, CAMK2G, OPRL1
IL-17A Signaling in Airway Cells	1.71	STAT3, NFKB2, IL17RA, CCL11, CXCL6
Role of IL-17A in Psoriasis	1.68	IL17RA, CXCL6
Prostanoid Biosynthesis	1.68	PTGS1, PTGS2
Role of Osteoblasts, Osteoclasts and Chondrocytes in Rheumatoid Arthritis	1.68	IL33, FZD4, IL1RL2, FRZB, IL1RL1, WNT2B, CHP1, IL1R1, SFRP1, WNT5A, BMP1
Protein Kinase A Signaling	1.67	AKAP12, PTPN13, PPP1R3C, CHP1, NFKB2, PRKAG1, PDE8A, PHKB, ADD3, PPP1R10, PDE7B, DUSP10, GNG5, PTGS2, CAMK2G, MTMR3
Atherosclerosis Signaling	1.67	IL33, VCAM1, LPL, SERPINA1, NFKB2, CCL11, F3
Remodeling of Epithelial Adherens Junctions	1.63	DNM1, TUBA1A, ARPC1B, DNM3, TUBA1B
PPARα/RXRα Activation	1.60	IL1RL2, IL1RL1, TGFB3, LPL, BCL3, IL1R1, NFKB2, RXRA, PRKAG1
Role of JAK family kinases in IL-6-type Cytokine Signaling	1.60	SOCS3, OSMR, STAT3
Nur77 Signaling in T Lymphocytes	1.59	HLA-DMA, CHP1, NR4A1, RXRA
IL-6 Signaling	1.59	IL33, SOCS3, IL1RL2, IL1RL1, STAT3, IL1R1, NFKB2
G-Protein Coupled Receptor Signaling	1.58	PDE8A, S1PR3, HRH2, PDE7B, CNR1, STAT3, NFKB2, AGTR2, AGTR1, PRKAG1, CAMK2G, OPRL1
Superpathway of Cholesterol Biosynthesis	1.51	FDFT1, TM7SF2, GGPS1
Hematopoiesis from Multipotent Stem Cells	1.51	KITLG, THPO
Oleate Biosynthesis II (Animals)	1.51	CYB5A, FADS1
γ-glutamyl Cycle	1.51	GCLM, ANPEP
Clathrin-mediated Endocytosis Signaling	1.45	DNM1, FGF21, ARPC1B, PIP5K1C, CHP1, DNM3, SERPINA1, FGF7, RAB4B
Amyloid Processing	1.44	CAPN1, BACE2, PRKAG1, PSEN1
Cardiac β-adrenergic Signaling	1.39	PDE8A, AKAP12, PPP1R10, PDE7B, PPP1R3C, GNG5, PRKAG1
Cholesterol Biosynthesis I	1.38	FDFT1, TM7SF2
Cholesterol Biosynthesis II (via 24,25-dihydrocholesterol)	1.38	FDFT1, TM7SF2
Cholesterol Biosynthesis III (via Desmosterol)	1.38	FDFT1, TM7SF2
Insulin Receptor Signaling	1.37	SOCS3, PPP1R10, SGK1, PPP1R3C, IRS2, NCK1, PRKAG1
Oxidative Phosphorylation	1.37	NDUFS5, COX10, NDUFA7, SDHD, CYB5A, UQCRCQ
Triacylglycerol Biosynthesis	1.36	PPAPDC1B, PPAP2B, AGPAT1
TREM1 Signaling	1.34	TLR2, CCL7, STAT3, NFKB2
VDR/RXR Activation	1.33	IL1RL1, VDR, CCL5, RXRA, SULT2A1
Role of JAK2 in Hormone-like Cytokine Signaling	1.32	SOCS3, IRS2, STAT3
Vitamin-C Transport	1.32	SLC2A1, GSTO1
Human Embryonic Stem Cell Pluripotency	1.31	S1PR3, FZD4, KLK3, WNT2B, PDGFRA, WNT5A, BMP1

Table S4. Related to Figure 5

Analysis of Pathways Regulated by Forskolin and A(70)-Bcl-2. Enrichment analysis of canonical pathways based on a set of 205 probe sets upregulated in both, MEF cultures treated with forskolin and MEF cultures expressing A(70)-Bcl-2 (each versus control cells, paired Limma test $p < 0.05$). All cells were transduced with an *Ascl1/RFP*- encoding vector. Analysis was done using Ingenuity Pathway Analysis software and significantly enriched terms ($p < 0.05$) are shown.

Supplemental Movies Legends

Movie S1. Related to Figure 1

Time-Lapse of the Effect of Bcl-2 During Neuronal Reprogramming

Video example showing 150 h of astroglia-to-neuron conversion of cultures transfected with plasmids encoding *Ascl1/RFP* (cells in white, left) or *Ascl1/RFP+Bcl-2* (cells in white, right; see Figure 1A and 2F for more details).

Movie S2. Related to Figure 1

DCX-GFP Reporter Expression in Ascl1- and Ascl1/Bcl-2-Mediated Reprogramming.

Video example showing 150 h of astroglia-to-neuron conversion of cultures co-transfected with the *Ascl1/RFP*- or *Ascl1/RFP+Bcl-2*-encoding plasmids (RFP is shown in white, right panels) and *DCX-GFP* (expression of GFP is shown in white, left panels).

Movie S3. Related to Figure 4

Time-Lapse of the Effect of Fk During Neuronal Reprogramming.

Video example showing neuronal conversion of astroglial cultures transfected with the plasmid encoding for *Ascl1/RFP* (cells in white) and tracked for 150 h. On the right, cells were additionally treated with Fk (20 μ M) 5 h before the tracking time started (See Figure 1A for more details). The last frames of the movie show immunostaining for RFP (red) and β -III-tubulin (green).

Supplemental Experimental Procedures

Transfection of Mouse Postnatal Astroglia Cultures

For transfection DNA-liposome complexes were prepared in Optimem medium (Invitrogen) using the retroviral plasmids described below and Lipofectamine 2000 (Invitrogen). Astrocyte cultures were exposed to DNA-liposome complexes at a concentration of 0.5 μ g DNA per 400 μ l of Optimem medium for 4 hours and cultured after that in the differentiation medium as above. See (Heinrich et al., 2011)

For survival analysis of transfected cells after immunostaining we counted the total number of RFP+ cells at 5 DPT and normalized by the total number of RFP+ cells counted at day 1. To quantify the ratio of neurons/initial transfected cells we counted the proportion of RFP+/ β -III-tubulin+ cells at 5 DPT and normalized by the whole population of RFP+ cells at 1 DPT.

Cell Cultures of Pericyte-Like Cells from Adult Human Cerebral Cortex

After removal of the meninges, tissue was dissected and dissociated mechanically. Subsequently, cells were centrifuged for 5 min at 1000 rpm, re-suspended, and plated in a medium consisting of DMEM high glucose with GlutaMAX (Gibco), 20% fetal calf serum (Gibco), penicillin/streptomycin (Gibco). For reprogramming experiments cells were harvested and replated as described above after 2-3 weeks of expansion. See also (Karow et al., 2012)

Cell Cultures of Mouse Embryonic Fibroblasts (MEFs)

MEFs were obtained from mouse embryos at day 14 gestation. Head, spine and viscera were removed and discarded (Vierbuchen et al., 2010). The remaining tissue was dissociated with 0.15% of trypsin, centrifuged for 5 min at 1300 rpm, re-suspended, and plated in a medium consisting of DMEM high glucose (3.5mM) with GlutaMAX (Gibco), 10% fetal calf serum (Gibco) and penicillin/streptomycin (Gibco) in 5% CO₂ and normoxxygenated conditions. Fibroblasts were used for experiments after minimum 3 passages. For reprogramming experiments cells were harvested and replated as described above for astrocytes.

Glycolytic and Oxidative Media

To force different metabolism during neuronal reprogramming, astrocytes were prepared and plated as previously described. At 24 hours after plating cells were either transfected with plasmid or infected with retroviral vectors and after further 24 hours medium was replaced with one of the following. (1) Control medium, composed of DMEM without sodium pyruvate or glucose (Gibco), supplemented with penicillin/streptomycin, B27 supplement (Gibco), glucose (4,5gr/l), sodium pyruvate (110mg/l); (2) Glycolysis-only (Glyco) medium, composed of DMEM without sodium pyruvate or glucose (Gibco), supplemented with penicillin/streptomycin, B27 supplement (Gibco), glucose (4,5gr/l), Oligomycin A (1 μ g/ml) (Gajewski et al., 2003). (3) Oxidative Phosphorylation-only (OxPhos) medium, composed of DMEM without sodium pyruvate or glucose (Gibco), supplemented with penicillin/streptomycin, B27 supplement (Gibco), sodium pyruvate (110mg/l), 2-Deoxy-D-glucose (5mM) (Candelario et al., 2013; Gajewski et al., 2003) .

Analysis of Redox State

To evaluate general ROS we used the CellRox Green reagent from Molecular probes that acquires green fluorescence and nuclear localization via DNA binding upon oxidation. The procedure was accordingly with the manufacturer's specifications and the green reporter was finally detected by microscopy of living cells stained with DAPI.

To detect ROS production from astrocytes in the different metabolic conditions, cells were loaded with the Dihydroethidium dye (DHE, life tech), a superoxide indicator that when oxidized intercalates within the cell's DNA, staining its nucleus a bright fluorescent red. After 24 hours in the metabolic medium, cells were incubated for 15 minutes with DHE (30 μ M) at 37°C, then washed 3 times in 1x phosphate-buffered saline (PBS), fixed with 4% PFA for 5 minutes and fluorescence was detected by microscopy (see below).

For *in vitro* experiments the antioxidants α Toc, Fk (Sigma) and/or calcitriol (Tocris) were supplemented once with the differentiation medium at 2 DPT/DPI in a final concentration of 0.5 μ M, 20 μ M and 70 μ g/ μ l, respectively.

Plasmids and DNA Constructs

For the expression of neurogenic transcription factors we used self-inactivating retroviral vectors containing the actin promoter with the cytomegalovirus early enhancer element and the splice acceptor of the rabbit beta-globin gene (pCAG) driving the expression of the gene of interest (flag/myc-*Ascl1*, flag-*Neurog2*, *Bcl-2* or *Dlx-2*) linked to a fluorescent reporter by internal ribosomal entry site (IRES) as previously described (Heinrich et al., 2011). To follow the conversion process of astrocytes into neurons, we used a neuronal reporter plasmid with GFP driven by the doublecortin promoter (*DCX-GFP*) previously described (Franco et al., 2011). The mouse version of *Bcl-2* cDNA was obtained from Source BioScience (IRAVp968H01145D; pCMV-SPORT6.1-*Bcl-2*) and the human cDNA version (h-*Bcl-2*) from addgene (Plasmid number 8793; pMIG-*Bcl-2*-IRES-GFP) to generate RV-pCAG-flag/myc-*Ascl1*-IRES-*Bcl-2*, RV-pCAG-flag-*Neurog2*-IRES-*Bcl-2* or RV-pCAG-*Bcl-2*-IRES-GFP, which encodes for both *Bcl-2* and the reporter GFP. The *Bcl-2* mutants A-*Bcl-2* and EE-*Bcl-2* were produced by directed mutagenesis with the oligos 5'-ggctgccaggacggctcctcagggccctcgttg-3' (and complementary) and 5'-gggacatggctgccaggaggagcctcagggccctcgttgcc-3' (and complementary) respectively, to generate the vectors pCMV-SPORT6.1-A-*Bcl-2*, RV-pCAG-*Ascl1*-IRES-A-*Bcl-2* and RV-pCAG-*Neurog2*-IRES-A-*Bcl-2* and the corresponding EE-*Bcl-2* versions. Mutations were verified by sequencing. The murine *Vdr* was obtained from Sino Biological (MG51106-G, Vector pGEM-T) and sub-cloned in the retroviral vector to generate RV-pCAG-*Vdr*-IRES-GFP.

Viral vectors were produced with a vesicular stomatitis virus pseudotyping at titers of 10^{6-9} and cells were infected about 24 hours after splitting as described above. Cells were allowed to differentiate in 16% O₂ and 9% CO₂.

Immunoblot Analysis

The cultures were lysed in RIPA buffer (10 mM Na₂HPO₄, pH 7.2, 150 mM NaCl, 1% sodium deoxicolate, 1% Nonidet P-40, 0.1% SDS) containing protease (Complete EDTA-free, Roche). Protein concentrations were determined with the BCA reagent from Interchim. Equal amounts of protein (50 μ g) were diluted in Laemmli Sample buffer containing β -mercaptoethanol (BioRad, 161-0747) and separated by polyacrylamide gel electrophoresis and transferred to polyvinylidene difluoride membranes (Pall; Life Sciences).

For the detection of *Prx1* the cells were previously incubated 15 min with PBS containing 100 mM N-ethylmaleimide (NEM, Sigma, E3876-5G) and collected in RIPA buffer also containing 100 mM NEM. In this case, samples were diluted in sample buffer without β -mercaptoethanol (Pierce, 84788).

Immunodetection of proteins was performed by standard procedures (ECL Prime Western Blotting Detection Reagent, Amersham).

Immunocytochemistry

Cells were fixed in 4 % PFA in PBS for 10 min at room temperature (RT), washed in PBS and pretreated in 0.5% Triton X-100 in PBS for 30 min, followed by incubation in 2% BSA and 0.5% Triton X-100 in PBS for 30 min. Primary antibodies were incubated on specimen overnight at 4°C in 2% BSA, 0.5% Triton X-100 in PBS. The following primary antibodies were used: polyclonal anti-Green Fluorescent Protein (GFP, chicken, 1:1000, Aves Labs, *GFP-1020*), polyclonal anti-Glial Fibrillary Acidic Protein (GFAP, rabbit, 1:4000, DakoCytomation, *Z0334*), polyclonal anti-Red Fluorescent Protein (RFP, rabbit, 1:500, Chemicon, *AB3216*, or 1:2000, Rockland *600-401-379*), monoclonal anti β -III-tubulin (mouse IgG2b, 1:500, Sigma, T8660), monoclonal anti Map2 (mouse IgG1, 1:500, Sigma, M4403), monoclonal anti NeuN (mouse IgG, 1:300, Millipore, MAB377), polyclonal anti V-Glut1 (rabbit, 1:500, SYSY, 135302), polyclonal anti synaptobrevin (SV, rabbit, 1:1000, SYSY). After washing in PBS, cells were incubated with appropriate species- or subclass-specific secondary antibodies conjugated to CyTM2, CyTM3, CyTM5 (1:500, Jackson ImmunoResearch), Alexa Fluor 488 (1:500, Invitrogen), FITC (fluorescein isothiocyanate, 1:500, Jackson ImmunoResearch), TRITC (tetramethyl rhodamine isothiocyanate, 1:500, Jackson ImmunoResearch) or biotin (1:500, Jackson ImmunoResearch or Vector Laboratories) for 2h in the dark at room temperature, followed by extensive washing in PBS. Following treatment with secondary antibodies conjugated to biotin, cells were subsequently incubated for 2h at room temperature with DAPI (1:1000, Sigma) and AMCA streptavidin (1:200, Vector Laboratories) or Alexa Fluor 647 streptavidin (1:500, Sigma, D9542) and mounted with Aqua Poly/Mount (Polysciences, Warrington, PA).

Luciferase assay

To test the activity of the Nrf2 pathway, we used a Nrf2-responsive luciferase construct obtained from Qiagen (kit CCS-5020). Accordingly with the described protocol, levels of Luciferase were normalized by the expression levels of a non-responsive construct encoding Renilla.

Immunohistochemistry

Animals were anesthetized and transcardially perfused with PBS, followed by 4% PFA in PBS. Brains were post-fixed overnight, washed twice with PBS and embedded in 4% agarose/water. Finally, 60µm-thick coronal sections were cut using a vibrating microtome (Leica).

For immunohistology, sections were pre-incubated for 30 min in blocking solution (2% bovine serum albumin, 0.5% Triton X-100 in PBS). The following primary antibodies were diluted in blocking solution and incubated with the sections for 48 hours at 4°C: chick anti-GFP (1:500, Aves Labs, GFP-1020), rabbit anti-RFP (1:500, Rockland, 600-401-379) or goat mCherry (1:250, Acris, AB0081-200), mouse anti-NeuN (1:250, Chemicon, MAB377), rat Ctip2 (1:250, Abcam, Ab18465), rabbit Cux1 (1:250, Santa Cruz, sc-13024), mouse Satb2 (1:250, Abcam, 51502), goat FoxP2 (1:250, Santa Cruz, sc-81069). After washing in PBS, secondary antibodies were diluted in blocking solution and incubated at room temperature for 2 hours. Such antibodies were chosen according to the primary ones and were coupled to Alexa Fluor 488 or FITC, Cy3, Alexa Fluor 647 (Dianova). Sections were eventually counterstained with DAPI (1:500, Sigma) prior to mounting.

RNA Extraction and Real Time Quantitative PCR (qRT-PCR)

RNA was extracted using RNeasy Plus Micro Kit (Qiagen) according to manufacturer's instructions, including removal of genomic DNA. RNA was retro-transcribed using SuperScriptIII Reverse Transcriptase and Random Primers (Roche). Each cDNA sample was diluted one to 5 and 1µl was used for each quantitative real time reaction. Real Time quantitative PCR (qPCR) was performed on a LightCycler480 instrument (Roche) using LightCycler Probe Master kit (Roche) and Monocolor Hydrolysis Probe (UPL) Probe (Roche) according to manufacturer's instructions (20µl final volume). The expression of each gene was analyzed in triplicate. Data were processed with the $\Delta\Delta C_t$ method (Livak and Schmittgen, 2001). Quantification was performed on 3 independent biological samples.

Microarray Analysis Procedure.

Total RNA (30 ng) was amplified using the Ovation Pico WTA System V2 in combination with the Encore Biotin Module (Nugen). Amplified cDNA was hybridized on Affymetrix Mouse Gene 2.0 ST arrays. Staining and scanning was done according to the Affymetrix expression protocol including minor modifications as suggested in the Encore Biotin protocol. Expression console was used for quality control and to obtain normalized RMA gene-level data. Statistical analyses were performed by utilizing the statistical programming environment R (Team, R. D. C., R: A language and environment for statistical computing. 2005) implemented in CARMAweb (Rainer et al., 2006). Genewise testing for differential expression was done employing the limma t-test. Sets of regulated genes were defined by $p < 0.01$ (507 probe sets) or $p < 0.05$ (1321 probe sets), including filters for fold change ≥ 1.5 x and average expression in at least one group in the dataset > 20 arbitrary units. Heatmaps were generated with CARMAweb and pathway enrichment analyses were generated through the use of IPA (Ingenuity® Systems, www.ingenuity.com).

Array data has been submitted to GEO under the accession number GEO: GSE70921

Microscopy

Immunostainings were analyzed with a LSM710 laser-scanning confocal or Axio Observer Z1 epifluorescence microscope (Carl Zeiss). Digital images were captured using the ZEN software (Carl Zeiss) and cell counts of all RFP/GFP immunoreactive cells performed with a 10X objective.

Live Imaging Microscopy Analysis

For quantifications, cells were tracked in every frame and proliferation, neuronal conversion or cell death was analyzed for every single cell in each movie. For quantification of proportion of dead neurons or astrocytes we counted cells dying as positive events and classified them as neurons or astrocytes according to their morphology described in Figure 1. Next we add to this value the number of surviving cells (astrocytes or neurons in each group) at the end of the tracking period. This result is the total population for each lineage (dead + surviving astrocytes or neurons). Finally we normalized the proportion of dead neurons (counted as described) to the total population of neurons (calculated as described) and the same process was done for astrocytes.

Patch-Clamp Method

Transfected GFP+ or RFP+ cells were recorded using the patch-clamp technique in the perforated-patch or whole-cell configurations. For the perforated-patch, fire-polished patch pipettes with 4-6 M Ω resistance were front-filled with intracellular solution containing Amphotericin B (0.33 μ g /ul) and backfilled with Amphotericin-free intracellular solution (in mM: 4 KCl, 2 NaCl, 0.2 EGTA, 135 K-Gluc, 10 HEPES, 4 ATP, 0.5 Na-GTP; pH = 7.3, 290 mOsm). Experiments were performed at room temperature with constant flow (2 ml/min) of the extracellular solution (in mM: 3 KCl, 140 NaCl, 2 CaCl₂, 2 MgCl₂, 10 HEPES, 5 Glucose; pH = 7.4, 305 mOsm). For the whole-cell configuration, the cells were kept in following extracellular solution (in mM: 125 NaCl, 3 KCl, 1.25 NaH₂PO₄, 25 NaHCO₃, 25 D-Glucose, 0.4 Ascorbic acid, 2 CaCl₂, 2 MgCl₂; pH = 7.4, 310-330 mOsm) oxygenated by 95% O₂/5% CO₂ with constant fluid flow (2ml/min) at room temperature. The cells were recorded at 5 days post-transfection in the whole-cell configuration (4-6 M Ω electrodes) with the following intracellular solution (in mM: 135 K-Gluconat, 4 KCl, 2 NaCl, 10 HEPES, 0.2 EGTA, 4 ATP, 0.5 NaGTP, 10 Phospho-Kreatin; pH = 7.3, 290-300 mOsm). The passive membrane properties were recorded using the membrane test paradigm of the pClamp software (Molecular Devices, Sunnyvale, CA, USA). In the voltage-clamp mode, a series of 10 mV rectangular pulse increments (50 ms long) ranging from -120 mV to +100 mV was used. Data were sampled at 10-30- μ s intervals and low-pass filtered at 2 kHz using the Axopatch 200B 4-pole Bessel filter (Molecular Devices). Leak currents were subtracted after the test pulse using five repeated 10 mV negative pulses from a holding potential of -120 mV. The current-voltage relation expressed the steady-state whole-cell current (at 40 ms of the rectangular pulse) as a function of the voltage command. In the current clamp, 1 second current injections of 10 pA increments were applied from 0 to 150 pA. All recorded cells were photographed both in the brightfield and the fluorescence using a CCD digital camera (Orca-D2, Hamamatsu, Herrsching, Germany).

Statistics

All error bars in this work indicate \pm SD. Statistical analyses were performed with GraphPad Prism 4 software by using t test or ANOVA with different post-hoc tests (Tukey's, Holm-Sidak's or Dunnett's). All the transfected cells from 3 coverslips were counted for each experiment with at least 3 independent experimental batches. Retroviral vector-transduced cells were quantified from five randomly chosen 10x fields in 3 different wells for each experiment in at least 3 independent experiments.

For *in vivo* experiments, pictures of the injected area were acquired with a confocal microscope (Zeiss) using 40x magnification. Cells infected by either one virus or both were quantified according to NeuN immunoreactivity, in animals treated and untreated with calcitriol or α -Tocotrienol, with the open-source software Fiji (<http://fiji.sc/Fiji>). The data were tested for significance using t test or two-way ANOVA analysis (no repeated measurements) with Tukey's correction for multiple comparisons (Prism 6, GraphPad). Asterisks in the plot represent multiplicity adjusted P-values.

Supplemental References

Candelario, K.M., Shuttleworth, C.W., and Cunningham, L.A. (2013). Neural stem/progenitor cells display a low requirement for oxidative metabolism independent of hypoxia inducible factor-1 α expression. *J Neurochem* 125, 420-429.

Franco, S.J., Martinez-Garay, I., Gil-Sanz, C., Harkins-Perry, S.R., and Muller, U. (2011). Reelin regulates cadherin function via Dab1/Rap1 to control neuronal migration and lamination in the neocortex. *Neuron* 69, 482-497.

Gajewski, C.D., Yang, L., Schon, E.A., and Manfredi, G. (2003). New insights into the bioenergetics of mitochondrial disorders using intracellular ATP reporters. *Mol Biol Cell* 14, 3628-3635.

Heinrich, C., Gascon, S., Masserdotti, G., Lepier, A., Sanchez, R., Simon-Ebert, T., Schroeder, T., Gotz, M., and Berninger, B. (2011). Generation of subtype-specific neurons from postnatal astroglia of the mouse cerebral cortex. *Nat Protoc* 6, 214-228.

Karow, M., Sanchez, R., Schichor, C., Masserdotti, G., Ortega, F., Heinrich, C., Gascon, S., Khan, M.A., Lie, D.C., Dellavalle, A., *et al.* (2012). Reprogramming of pericyte-derived cells of the adult human brain into induced neuronal cells. *Cell Stem Cell* 11, 471-476.


Rainer, J., Sanchez-Cabo, F., Stocker, G., Sturn, A., and Trajanoski, Z. (2006). CARMAweb: comprehensive R- and bioconductor-based web service for microarray data analysis. *Nucleic Acids Res* 34, W498-503.

Vierbuchen, T., Ostermeier, A., Pang, Z.P., Kokubu, Y., Sudhof, T.C., and Wernig, M. (2010). Direct conversion of fibroblasts to functional neurons by defined factors. *Nature* 463, 1035-1041.



[Click here to access/download](#)

Supplemental Movies & Spreadsheets
Movie S1.mp4



[Click here to access/download](#)

Supplemental Movies & Spreadsheets
Movie S2.mp4



[Click here to access/download](#)

Supplemental Movies & Spreadsheets
Movie S3.mp4